Generation of 21-fs Pulses from a Cr:LiSAF Laser Mode Locked with a Single-Walled Carbon Nanotube Saturable Absorber

by

Gökhan Tanısalı

A Dissertation Submitted to the

Graduate School of Sciences and Engineering

in Partial Fulfilment of the Requirements for

the Degree of

Master of Science

in

Physics

KOÇ ÜNİVERSİTESİ

January 17, 2020

Generation of 21-fs Pulses from a Cr:LiSAF Laser Mode Locked with a Single-Walled Carbon Nanotube Saturable Absorber

Koç University

Graduate School of Sciences and Engineering

This is to certify that I have examined this copy of a master's thesis by

Gökhan Tanısalı

and have found that it is complete and satisfactory in all respects,

and that any and all revisions required by the final

examining committee have been made.

Committee Members:

Prof. Dr. Alphan Sennaroğlu (Advisor)

Prof. Dr. Alper Kiraz

Assoc. Prof. Dr. Ümit Demirbaş

Date:

ABSTRACT

Generation of 21-fs Pulses from a Cr:LiSAF Laser Mode Locked with a Single-Walled Carbon Nanotube Saturable Absorber

Gökhan Tanısalı

Master of Science in Physics

January 17, 2020

Single-walled carbon nanotube saturable absorbers (SWCNT-SAs) possess many favourable nonlinear optical properties over a wide range of wavelengths, such as strong absorption saturation, low non-saturable losses, short recovery times, and low-cost fabrication schemes. These properties have made SWCNT-SAs viable alternatives to semiconductor saturable absorber mirrors (SESAMs) for the mode locking of solid state and fiber lasers over a very broad wavelength range.

In this thesis, the aim was to demonstrate the ultrashort pulse generating capability of SWCNT-SAs. First, the characterization of the SWCNT-SA used in the experiments was conducted. The absorption of the SWCNT-SA was measured to be around 2% at 850 nm, which is the free-running wavelength of Cr:LiSAF lasers. After performing pump-probe spectroscopy, the fast and slow decay times of the SWCNT-SA were measured to be 0.4 and 2.7 ps. The saturation fluence and the single pass modulation depth of the SWCNT-SA were further determined to be 45 $\mu J/cm^2$ and 0.3%, respectively. To test the ultrashort pulse generating capability of the SWCNT-SA, a Cr:LiSAF laser was chosen since it has a broad emission band, enabling the generation of ultrashort pulses with femtosecond duration. In the experiments, the Cr:LiSAF laser was pumped with 210 mW of pump power with two low-cost, low-power diode lasers at 660 nm, and produced around 9 mW of mode-locked output power centered around 875 nm. The pulse duration of 21 fs, which was achieved during the experiments, represents the shortest pulses directly generated from a SWCNT-SA mode-locked solid-state laser. The pulse repetition rate was 47.9 MHz with a pulse energy of 0.18 nJ and peak pulse power of 9 kW. The time-bandwidth product of the produced pulses was 0.56. Kerr lens mode locking

experiments were further conducted to test if the SWCNT-SA puts any limitation on the obtainable pulse duration. The experiments clearly showed that the obtainable pulse duration was not limited by the SWCNT-SA.

Furthermore, the continuous-wave operation of the Cr:LiSAF laser at 850 nm was experimentally investigated in detail. Accurate measurements of the transmissions of the output couplers used in the experiments were conducted. Then for the Cr:LiSAF laser constructed with different output couplers, the threshold pump power and power efficiency data were measured while the laser was tuned to operate exactly at 850 nm by using an intracavity tuning prism. The data taken enabled a complete experimental characterization of the continuous-wave Cr:LiSAF laser and provides useful guidelines for the construction of similar laser systems.

ÖZETÇE

Tek Duvarlı Karbon Nanotüp Doyabilen Soğurucuları ile Kip Kilitlenmiş Cr:LiSAF Lazerinden 21 fs Darbe Üretimi

Gökhan Tanısalı

Fizik, Yüksek Lisans

17 Ocak 2020

Tek duvarlı karbon nanotüp doyabilen soğurucuları, geniş dalga boyu aralığında, yüksek soğurma satürasyonu, düşük satüre olamayan kayıplar, kısa sönüm süresi ve düşük maliyetli üretim teknikleri gibi birçok faydalı özelliğe sahiptir. Bu özellikler katı hal ve fiber lazerlerinin kip kilitlenmesinde tek duvarlı karbon nanotüp doyabilen soğurucuları, yarı iletken doyabilen soğurucu aynalara karşı uygun bir alternatif haline getirmiştir.

Bu tezin asıl amacı tek duvarlı karbon nanotüp doyabilen soğurucuların çok kısa darbe üretme kapasitelerini test etmektir. İlk olarak, deneylerde kullanılan tek duvarlı karbon nanotüp doyabilen soğurucuların karakterizasyonu yapılmıştır. Tek duvarlı karbon nanotüp doyabilen soğurucunun, Cr:LiSAF lazerinin çalıştığı dalga boyu olan 850 nm'deki soğurma miktarı yaklaşık %2 olarak ölçülmüştür. Pompa - sonda spektroskopisiyle tek duvarlı karbon nanotüp doyabilen soğurucunun hızlı ve yavaş sönüm süreleri 0.4 ve 2.7 ps olarak ölçülmüştür. Tek duvarlı karbon nanotüp doyabilen soğurucunun doyma akısı ve tek geçiş modülasyon derinliği 45 μJ/cm^2 and 0.3% olarak belirlenmiştir. Tek duvarlı karbon nanotüp doyabilen soğurucunun kısa darbe üretme kapasitesini test etmek için geniş ışıma bandına sahip olduğundan femtosaniye darbe üretmeye imkan veren Cr:LiSAF lazeri seçilmiştir. Deneyler sırasında, Cr:LiSAF lazeri düşük maliyetli, düşük güçlü iki diyotla 660 nm'de 210 mW pompa gücüyle pompalanmış ve 875 nm civarında 9 mW güç üretmiştir. Deneyler sırasında elde edilen 21 fs süreli darbeler, tek duvarlı karbon nanotüp doyabilen soğurucularla kip kilitlenmiş katı hal lazerlerinden direkt olarka üretilen darbeler arasında en kısa olanıdır. 0.18 nJ enerji ve 9 kW güce sahip darbelerin tekrarlama frekansı 47.9 MHz'dir. Üretilen

darbelerin zaman – bant aralığı çarpımı 0.56’dır. Ayrıca tek duvarlı karbon nanotüp doyabilen soğurucunun üretilen darbe süresi üzerinde bir sınırlamada bulunup bulunmadığını test etmek için Kerr odaklamalı kip kilitleme deneyleri de yapılmıştır. Bu deneyler, elde edilebilen darbe süresinin tek duvarlı karbon nanotüp doyabilen soğurucu tarafından sınırlanmadığını açıkça göstermiştir.

Buna ek olarak, Cr:LiSAF lazerinin 850 nm’de sürekli dalga çalıştırılışı da detaylıca incelenmiştir. Deneylerde kullanılan çıkış aynalarının geçirgenlik değerlerinin ölçümleri yapılmıştır. Daha sonra farklı çıkış aynaları ile kurulan Cr:LiSAF lazerinin eşik pompa güçleri ve verim eğrileri lazer dalgaboyu rezonatör içi prizma kullanılıp 850 nm’ye ayarlanarak ölçülmüşür. Ölçülen bu değerler sürekli dalga Cr:LiSAF lazerinin eksiksiz deneysel karakterizasyonunu mümkün kılmıştır ve benzer lazer sistemlerinin kurulumu için yol gösterici olabilir.

ACKNOWLEDGEMENTS

I would like to say thanks to my advisor, Alphan Sennaroğlu, for providing me with the opportunity to work in Laser Research Laboratory in the first year of my university life, the last year of my undergraduate study and during my master study. In that sense, it is especially pleasing for me to graduate from a laboratory where I started with in my first year in the university as a novice student. I am indebted to my advisor for guiding me throughout my research and many soft skills that I acquired from him over the course of my studies here.

I am also grateful to Adnan Kurt for his support during my experiments, and his willingness to help me in my research. I cannot imagine how worse it could get when my diodes burned out if I do not know him.

I am pleased to thank Ümit Demirbaş for his collaboration and allocating his time to be in my thesis committee. I also present my appreciation to Alper Kiraz for being in my thesis committee.

I want to thank current and previous labmates. I want to thank Işınsu Baylam for helping me to carry out the main experiments of this thesis at late nights. I want to thank Ferda Canbaz for being my first mentor in the lab. I want to thank Abdullah Muti for all the fun time we had and inside jokes almost nobody understands. I also want to thank him for helping me in the day when my experiments started working after a long time of unsuccessful trials. He may not even remember this, but it meant a lot to me. Yağız Morova deserves special thanks for helping me to tackle with all kinds of bureaucratic obstacles, his fun conversations, and being a good companion to me in video games.

Lastly, I want to thank Fulya Akşit for her unconditional and unmatched support for me since almost the first day I met her. I want to send my appreciation to my father for raising me in the way he did, and my mother for her permanent support. My sister Nihan also deserves special thanks for being such an uncritical person and my lifelong companion.

Table of Contents

LIST OF TABLES

LIST OF FIGURES

Chapter 1
INTRODUCTION

During this thesis study, the emphasis was on two experimental studies, namely the continuous wave and pulsed operation of Cr:LiSAF laser, as discussed in Chapter 2 and Chapter 3, respectively. Chapter 2 investigates the continuous-wave operation of Cr:LiSAF laser by measuring the power efficiency data and threshold values. It concludes with a short analysis of the experimental data. Chapter 3 discusses the mode-locked operation, a method to generate pulses, of Cr:LiSAF laser with single-walled carbon nanotube saturable absorbers (SWCNT-SA). It starts with the characterization of the SWCNT-SA used in the experiments, and then presents the mode-locking experiments, and the characteristics of the produced pulses. Chapter 1 touch upon the main pieces of information required to grasp the work done during this thesis. For this purpose, Chapter 1 starts with a section that provides a short literature survey of Cr:LiSAF lasers, and its spectroscopic characteristics in terms of a lasing material. In Section 1.2, this is followed by the classification of SWCNT-SAs, their optical properties as mode-lockers, and previous works in which they have been used. After the qualitative discussion on the two main components of the experiments conducted during this thesis, Cr:LiSAF lasers and SWCNT-SAs, a basic quantitative analysis of ideal four-level solid-state lasers is given in Section 1.3 since Cr:LiSAF lasers can be modelled as one. Section 1.4 introduces and derives important concepts, such as gain, threshold power and efficiency of a laser, starting with the rate equations developed in Section 1.3. However, the steady state analysis of a laser cannot account for the mode locking experiments discussed in Chapter 3, and for this reason, Section 1.5 gives a short overview of pulse generation through mode locking. Section 1.6 describes the propagation of pulses in dispersive media, and how this distorts the pulse shape. It is quite relevant to this study, where 21-fs pulses were obtained, since the distortions become more apparent as the pulse duration gets shorter. Finally, Section 1.7 is devoted to the measurement of pulse durations using a home-built interferometric autocorrelator.

1.1 Cr:LiSAF Lasers

The gain medium of the laser constructed to perform experiments for this thesis work was Cr^{3+}:$LiSrAIF_6$ (Cr:LiSAF), and the main reason behind this is its short pulse generating capability. Also, they are low-cost, low power lasers, which can even be battery-powered. This becomes especially important when it comes to build portable devices for specific applications such as biomedical imaging [1]. Therefore, in this section, the reader will be first introduced to the historical overview of Cr:LiSAF lasers and the milestone experiments. In the second part, spectroscopic and thermal properties of Cr:LiSAF gain medium will be given in comparisons with other gain media.

The first demonstration of Cr:LiSAF dates back to 1989 in Lawrance Livermore National Laboratory by Stephan A. Payne and his colleagues [2]. In this first demonstration, Payne et al. pumped the Cr:LiSAF sample with a Kr laser and obtained the slope efficiency of 36%. They were also able to tune the laser from 780 to 920 nm [2]. Cr:LiSAF lasers have an important advantage that they can be pumped by diode lasers, and the first demonstration of this was published by Scheps et al. in 1991 [3]. In 1992, the first mode-locking of Cr:LiSAF laser was achieved by Miller et al. [4], where they obtained 150-fs long pulses using Kerr-lens mode locking (KLM) aided by an acousto-optic modulator. In the same year, Evans et al. achieved to produce 50-fs pulses from an Ar laser pumped, KLM mode-locked Cr:LiSAF laser without a need for an acousto-optic modulator to sustain the pulses [5]. Another important leap forward occurred in 1997, when Valentine et al., using a single narrow-stripe laser diode as a pump source, demonstrated the generation of femtosecond pulses from a Cr:LiSAF laser for the first time [6]. They were able to obtain stable 75-fs pulses with only 36 mW of incident pump power. This low threshold laser configuration led to a portable, battery-powered, low-cost Cr:LiSAF laser systems [7-13]. In 1999, Uemura and Torizuka, using Kerr-lens mode locking, obtained 12-fs pulses from a Cr:LiSAF laser [14], which is followed by the generation of the shortest pulses (10 fs) from a Cr:LiSAF laser in 2000 [15]. Carbon nanotube mode-locked Cr:LiSAF laser was first demonstrated in 2012 by Agnesi et al., where they achieved 122-fs pulses at the average output power of 16 mW, and a tuning range of 14 nm with a single diode pumping scheme [16]. A mode locked Cr:LiSAF with graphene saturable absorber was first demonstrated in 2014 by Canbaz et al. [17], and later in 2017, by the same group, 19-fs pulses were obtained from a graphene saturable absorber mode locked Cr:LiSAF laser [18].

The energy level diagram of the Cr^{3+}:LiSAF lasers is shown in the Figure 1-1. Pumped ions from the $^4A_2$ state to upper $^4T_2$ decay to the bottom of the $^4T_2$ state via ^2E energy level. Laser transition occurs from the bottom of the $^4T_2$ state to the excited vibrational states, where the non-radiative transition brings ions back to the ground level $^4A_2$. This is a four-level laser where three electronic states and one vibrational level are involved. There are also energy degrading mechanisms of excited state absorption taking place between $^4T_2$ to $^4T_1$a states, and Auger-type energy transfer upconversion [19, 20].

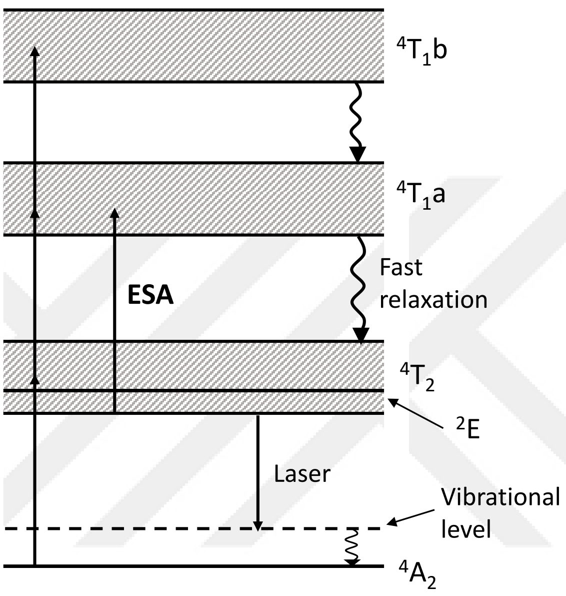

Figure 1-1. Energy levels of low field Cr3+ ion showing optical transitions during pumping, lasing and ESA (adopted from [21]).

The absorption and emission spectra of Cr:LiSAF lasers for the π-polarization ($E||c$) and σ-polarization ($E\perp c$) are given in Figure 1-2. The three peaks at the absorption spectra with the order of increasing wavelength arise from the transitions $^4A_2 \rightarrow {}^4T_1$b, $^4T_1$a and $^4T_2$, respectively. The broadband absorption of Cr:LiSAF enables it to be pumped by both flashlamps and low-cost red diodes around 650 nm. The emission of Cr:LiSAF is strongly π-polarized, hence the c axis of the gain medium should be placed perpendicular to the direction of the optical axis. As can be seen from the emission wavelength in Figure 1-2, and previous studies [2, 21, 22] the tuning range of Cr:LiSAF extends from 760 nm to 1110 nm. The broad emission band makes Cr:LiSAF ideal for short pulse generation [15, 18, 23].

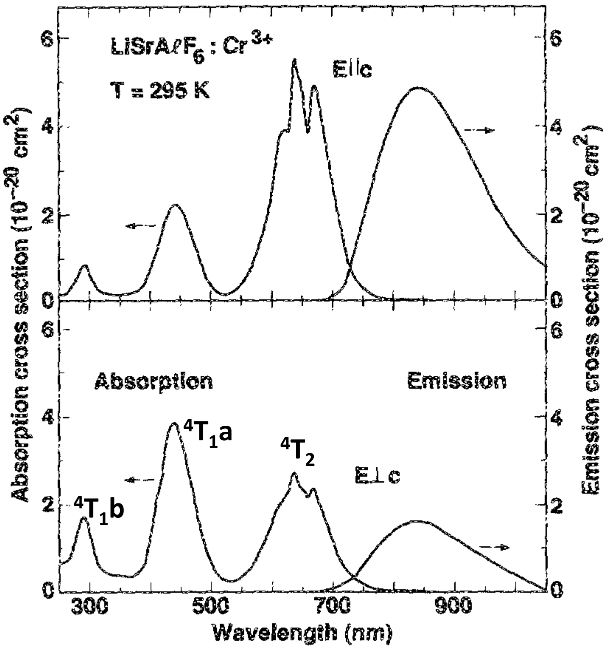

Figure 1-2. Absorption and emission spectra of Cr:LiSAF lasers for the π-polarization (E||c) and σ-polarization (E⊥ c) (taken from [2])

The peak emission cross section of Cr:LiSAF is 4.8×10^{-20} cm^2, which is significantly lower than Ti^{3+}:sapphire laser operating in similar wavelength ranges with Cr:LiSAF [24]. On the other hand, fluorescence lifetime of Cr:LiSAF is quite high (67 μs), yielding a relatively high emission cross section and fluorescence lifetime product ($\sigma_e \tau_f = 322 \times 10^{-20}$ cm^2- μs) [24]. Due to this high value of emission cross section and fluorescence lifetime product Cr:LiSAF lasers have very low threshold values.

Another important property of gain media is their thermal properties, which is especially relevant at high average power or high pulse power operations. High fracture toughness, high thermal conductivity and low thermal expansion coefficient make a gain medium suitable for high power operations. Cr:LiSAF performs quite poor in terms of thermal properties compared to, for example, Ti^{3+}:sapphire gain media. Therefore, it would be more appropriate to compare the thermal properties of Cr:LiSAF with those of glass, which are given in Table 1-1. On the other hand, thermally induced refractive index change in Cr:LiSAF is quite low ($dn/dT = -4 \times 10^{-6}\ K^{-1}$) [25] in comparison with oxide crystals, which enables better beam quality at high powers. Note also that low nonlinear refractive index of the Cr:LiSAF gain medium ($0.8 \times 10^{-16}\ cm^2/W$) [25], together with its negative thermal lensing, poses problem in obtaining KLM.

Table 1-1. Comparison of thermal and mechanical properties of Cr:LiSAF and glass (taken from [26])

	Cr:LiSAF	Glass
Thermal shock resistance ($W/m^{1/2}$)	≈0.4	≈0.4
Fracture strength (kg/mm^2)	3.9	5
Thermal expansion coefficient (×10−6/^{0}C)	22	11.4
Young's modulus (Gpa)	100	50
Microhardness (kg/mm^2)	197	≈500
Fracture toughness ($MPam^{1/2}$)	0.4	0.45
Thermal conductivity ($W/m^{-1}K^{-1}$)	3.09	0.62

1.2 Single-Walled Carbon Nanotubes Saturable Absorbers

For passive mode locking operations of lasers, saturable absorbers, such as single-walled carbon nanotubes (SWCNT-SAs), graphene saturable absorbers or semiconductor saturable absorber mirrors, have to be employed. In the mode locking experiments conducted for this thesis work (See Chapter 3), a SWCNT-SA was used to test its pulse generating capabilities. This section starts with introducing the concept of chirality which determines the optical properties of carbon nanotubes. It further discuss the advantages of SWCNT-SAs as mode-lockers over SESAMs and gives a short list of previous studies spanning the whole wavelength range in which SWCNTs has been used.

Carbon nonotubes were discovered by Sumio Iijima in 1991 [27], and since then it has attracted attentions of scientists and engineers both for basic and applied research. Carbon nanotubes can be visualized as hollow cyclinders, and they are formed by rolling honeycomp lattice of graphene (See Figure 1-3(a)). Two hexagons in the lattice have to be overlapped when the lattice is rolled into a tube. As can be seen from the Figure 1-3(b), the vector connecting the center of these two hexagons is called the chiral vector $\boldsymbol{C}$, and can be shown as $\boldsymbol{C} = n\boldsymbol{a_1} + m\boldsymbol{a_2}$, where $\boldsymbol{a_1}$ and $\boldsymbol{a_2}$ are the basis vectors of the graphene lattice and, the two integers (n,m) are called the chirality of the carbon nanotube. The angle θ subtended by the chiral vector $\boldsymbol{C}$ and the basis vector $\boldsymbol{a_1}$ determines the electronic properties of the carbon nanotubes, and is given by

$$\cos\theta = \frac{\boldsymbol{C}.\boldsymbol{a_1}}{|\boldsymbol{C}||\boldsymbol{a_1}|} = \frac{2n+m}{2\sqrt{n^2+m^2+nm}} \qquad 1\text{-}1$$

The nanotube diameter is found by

$$d_t = \frac{|\boldsymbol{C}|}{\boldsymbol{\pi}} = \frac{a_{C-C}}{\boldsymbol{\pi}}\sqrt{3(n^2+m^2+nm)} \tag{1-2}$$

where $a_{C-C} \approx 1.44$ Å is the distance between the adjacent carbon atoms in graphene. The diameters of carbon nanotubes are usually in the range of 1-3 nm [28], while their lengths can be up to millimetres [29].

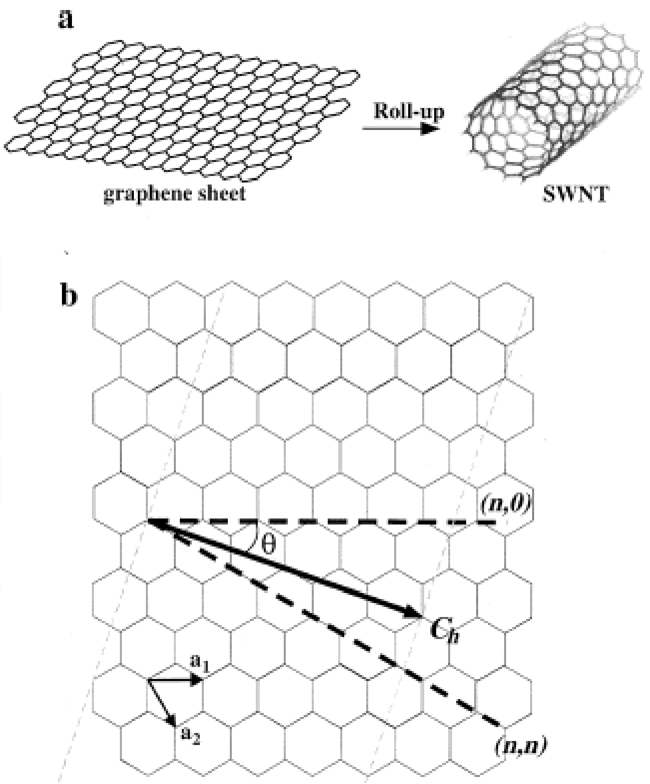

Figure 1-3. (a) A graphene is rolled to form a SWCNT. (b) Basis vectors $\boldsymbol{a_1}$ and $\boldsymbol{a_2}$, zigzag (m=0), armchair (n=m), and chiral vector are shown on graphene lattice (taken from [30])

Based on their chirality, carbon nanotubes can be classified into three groups,

1. Zigzag nanotubes for which m=0. The dashed line with (n,0) in Figure 1-3(b) demonstrates zigzag carbon nanotube.
2. Armchair nanotubes for which n = m. The dashed line with (n,n) in Figure 1-3(b) demonstrates the armchair carbon nanotube.
3. Chiral nanotubes for which n ≠m ≠ 0.

Whether a SWCNT is metallic or semiconducting can be determined from its chirality. For $n - m = 3l$, where l is a nonnegative integer, the SWCNT exhibits metallic properties and for all the other n and m values it exhibits semiconducting properties. All metallic and semiconducting SWCNTs are respectively shown with red solid points and hallow circles in the chirality map in Figure 1-4.

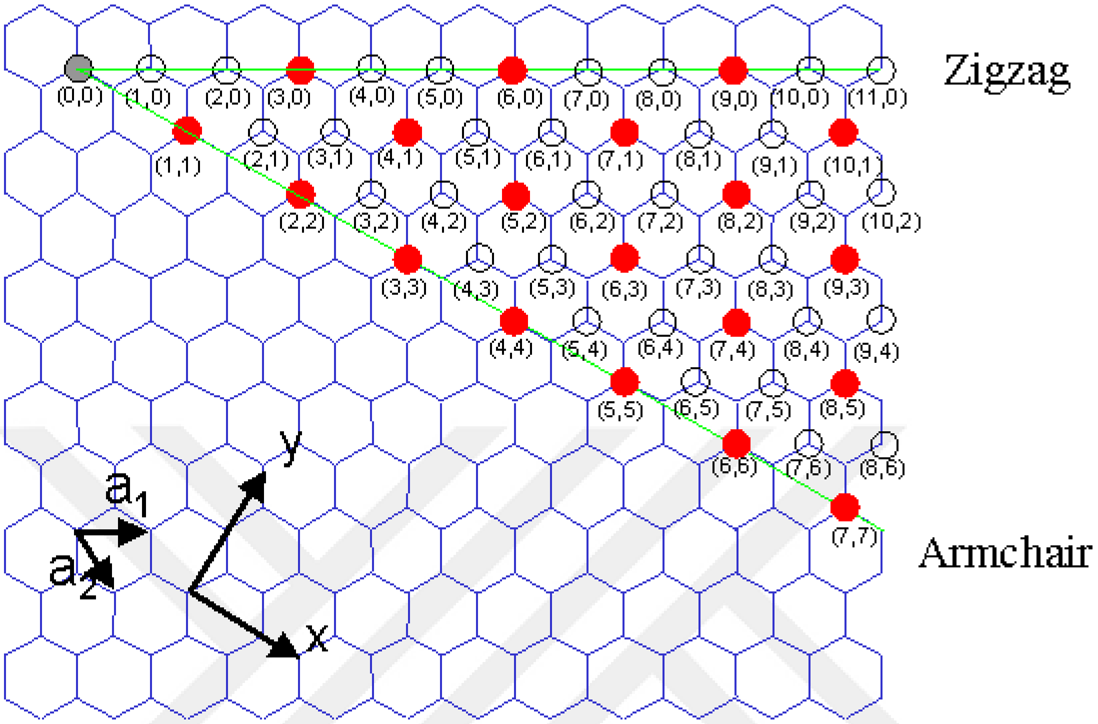

Figure 1-4. Chirality map of SWCNTs. If the hexagon (0,0) is rolled onto any of the blue hexagons the SWCNT exhibits metallic properties, if rolled onto any of the yellow hexagons the SWCNT exhibits semiconducting properties. Also note that zigzag and armchair carbon nanotubes have a chiral angle of 0^0 and 30^0, respectively [31].

As for single-walled carbon nanotube saturable absorbers (SWCNT-SAs), they are promising alternatives to semiconductor saturable absorber mirrors (SESAM) for the generation of ultrashort pulses. It is easier to adjust absorption bands of the SWCNT-SA in the infrared region by tuning the diameter and the chirality of carbon nanotubes [32]. However, each SESAM operates in a narrow nonlinear absorption band and requires complex manufacturing techniques to be functional in femtosecond pulse generations [32]. On the other hand, a single SWCNT-SA device on which a mixture of carbon nanotubes having different diameter and chirality are present can exhibit a broad absorption band of over 500 nm [32]. Figure 1-5 shows the transmission of SWCNT-SAs with different chiralities. High damage threshold, low non-saturable losses, low saturation fluence and short recovery time of SWCNT-SAs make them suitable for femtosecond pulse generation.

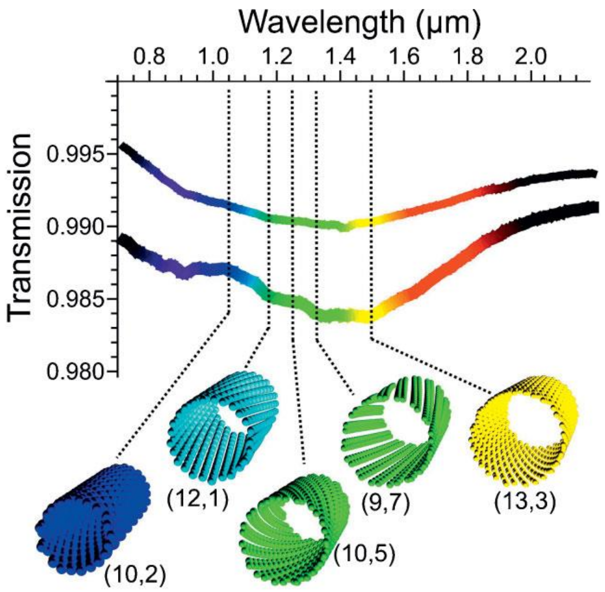

Figure 1-5. Transmission spectra of two SWCNT-SA with different densities. For each SWCNT-SA with different chiralities (n,m), the absorption wavelength was determined from Raman spectroscopy and indicated with dashed lines (taken from [32]).

SWCNT-SAs have been used to generate mode-locked output from solid-state and fiber lasers operating between 800 and 2870 nm [32-40]. To date, among the experiments performed with SWCNT-SA mode-locked solid-state and fiber lasers, the directly generated shortest pulses have a duration of 21 fs [23].

1.3 Rate Equations of Ideal Four-Level Solid-State Lasers

Cr:LiSAF lasers are four-level laser systems, hence it is appropriate to discuss the rate equations for ideal four-level systems. This section is based on the Ref. [41].

The schematic representation of the ideal four-level atom is given in the Figure 1-6 below. In the absence of optical pumping, all the atoms reside at the ground state $|g\rangle$. Optical pumping excites those atoms to the pump band $|3\rangle$, where fast radiative decay takes the them to the upper laser level $|2\rangle$. Both spontaneous and stimulated emission occur from upper laser level $|2\rangle$ to lower laser level $|1\rangle$. The atoms in level $|1\rangle$ again undergo fast nonradiative decay to the ground state $|g\rangle$. Since the lifetime of the atoms at the states $|1\rangle$ and $|3\rangle$ are significantly shorter than lifetimes at the state $|2\rangle$, it is assumed that N_1 and N_3 (population densities at $|1\rangle$ and $|3\rangle$) are negligible. Therefore, the population density of the upper laser level N_2 takes the form

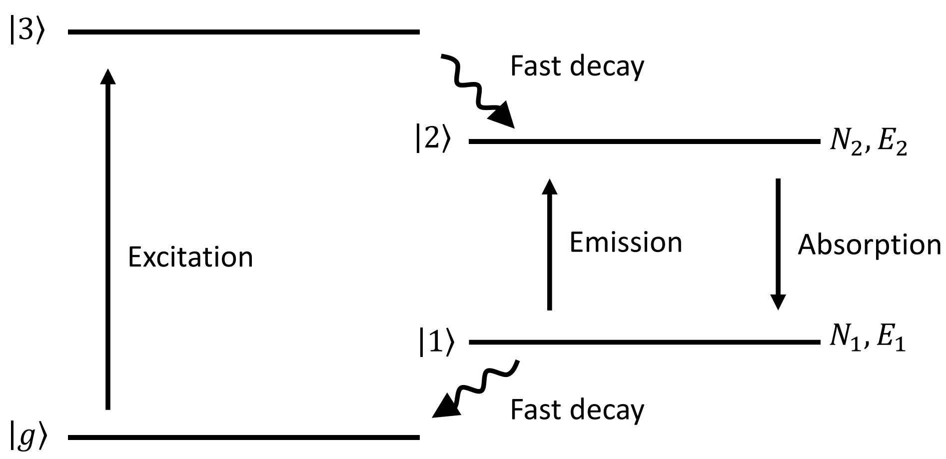

Figure 1-6. Energy level diagram of an ideal four-level atom.

$$\frac{dN_2}{dt} = \frac{\sigma_a I_p}{h\nu_p} N_g - \frac{N_2}{\tau_f} - \frac{\sigma_e I_L}{h\nu_L} N_2 \qquad 1\text{-}3$$

with

$$N_g + N_2 = N_T \qquad 1\text{-}4$$

where I_p is the pump intensity at the pump wavelength of λ_p, I_L is the laser intensity at the lasing wavelength of λ_p, σ_a and σ_e are the absorption and stimulated emission cross sections, τ_f is the fluorescence lifetime of level $|2\rangle$, h is the Planck constant, N_g and N_T are the ground-state and total population densities, ν_p and ν_L are the pump and laser frequency.

1.4 Steady State Analysis of Ideal Four-Level Solid-State Lasers

Using the rate equations for ideal four-level lasers developed in the previous section, steady state, continuous-wave analysis of lasers will be given. Several concepts, including gain, threshold power, efficiency will be introduced, and they will be expressed as relevant laser parameters. This section is based on the Ref. [41].

With the assumption that the gain medium is thin, the fractional power gain G per pass through the gain medium can be defined as

$$G = \frac{\Delta P_L}{P_L} \qquad 1\text{-}5$$

where P_L is the laser power and ΔP_L is the change in the laser power after a single pass through the gain medium. It can be shown that

$$G = \sigma_e N_2 d_g \qquad 1\text{-}6$$

where d_g is the length of the gain medium. Assuming pump absorption is negligible, multiplying both sides of the Eq. (1-3) with $\sigma_e d_g$ yields

$$\frac{dG}{dt} = -\frac{G(t) - G_0}{\tau_f} - \frac{P_L G(t)}{E_{sL}} \qquad 1\text{-}7$$

Here E_{sL} is the saturation energy given by

$$E_{sL} = \frac{h\nu_L}{\sigma_e} a_L \qquad 1\text{-}8$$

where a_L is laser beam area, and G_0 is the small-signal fractional power gain given by

$$G_0 = \frac{\sigma_a I_p N_g}{h\nu_p} \sigma_e d_g \tau_f \qquad 1\text{-}9$$

In the case of steady state, continuous wave regime, time rate of change of G is zero. Therefore, Eq. (1-7) takes the form

$$G_s = \frac{G_0}{1 + \frac{P_L}{P_{sL}}} \qquad 1\text{-}10$$

where P_{sL} is the saturation power at the lasing wavelength which can be written as

$$P_{sL} = \frac{E_{sL}}{\tau_f} = \frac{h\nu_L}{\sigma_e \tau_f} a_L \qquad 1\text{-}11$$

G_s is the steady-state fractional power gain per pass, and can also be expressed as

$$G_s = G_{th} = \frac{1}{2}(L + T) \qquad 1\text{-}12$$

where G_{th} stands for the threshold gain, L is the total round trip loss of the cavity, and T is the output coupler transmission. G_{th} is the single pass power gain through the amplifier, which is just enough gain for a laser resonator to lase. To provide an intuitive insight for Eq. (1-12), note that a laser resonator has to overcome attenuation of intracavity power due to the losses and output coupler transmission. Therefore, threshold power gain per pass should be equal to the half the total intracavity loss and output coupler transmission. Once the threshold gain is exceeded by increasing the pump power, the gain eventually saturates back to the threshold gain. Otherwise, the intracavity laser power would increase indefinitely, which is not possible. Therefore, in the steady state regime, G_s has to be equal to G_{th}.

Substituting Eq. (1-9) and (1-11) into Eq. (1-10), P_L can be found as

$$P_L = \frac{\frac{\sigma_a N_T}{h\nu_p}\sigma_e d_g \tau_f h\nu_l P_p - h\nu_l a_L G_s}{\sigma_e \tau_f G_s} \qquad 1\text{-}13$$

Efficiency and threshold power of an ideal for level system can be found using Eq. (11). By definition, efficiency η can be expressed as

$$\eta = \frac{\partial P_L}{\partial P_p} \qquad 1\text{-}14$$

Using Eq. (1-13) and (1-14),

$$\eta = \frac{\partial P_L}{\partial P_p} = \frac{T}{T+L}\frac{\lambda_p}{\lambda_L}\sigma_a N_T d_g \qquad 1\text{-}15$$

Product $\eta_a = \sigma_a N_g d_g \approx \sigma_a N_T d_g$ is the fractional pump absorption. In the ideal case of 100% pump absorption and no loss, the efficiency is given by λ_p/λ_L, which is known as the quantum efficiency of a laser.

Threshold power of a laser can also be found by using Eq. (1-13) because as $P_L \rightarrow 0$, $P_p \rightarrow P_{th}$. Hence,

$$P_L = \frac{\frac{\sigma_a N_T}{h\nu_p}\sigma_e d_g \tau_f h\nu_l P_p - h\nu_l a_L G_s}{\sigma_e \tau_f G_s} \rightarrow 0 \qquad 1\text{-}16$$

as long as

$$P_p \rightarrow \frac{h\nu_l a_L G_s}{\frac{\sigma_a N_T}{h\nu_p}\sigma_e d_g \tau_f h\nu_l} \qquad 1\text{-}17$$

Substituting Eq. (1-12) for G_s in Eq. (1-17), and denoting all the constants with A, threshold power can be written as

$$P_{th} = A(L + T) \qquad 1\text{-}18$$

From Eq. (1-15) and (1-18), for any pump power greater than threshold pumping level, output power of an ideal four-level laser system can be found as

$$P_{out} = \eta(P_p - P_{th}) \qquad 1\text{-}19$$

as shown in Figure 1-7.

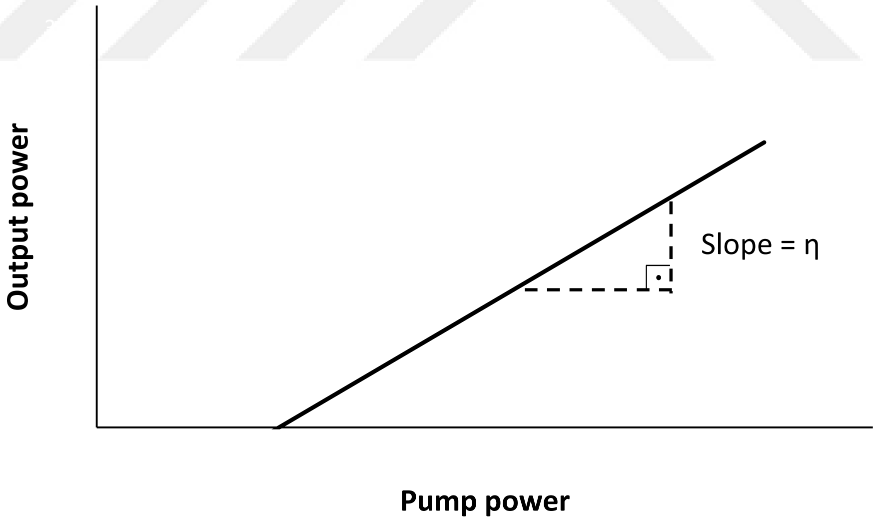

Figure 1-7. Output power of a laser as a function of pump power.

1.5 Mode-Locked Operations of Lasers

There are several ways to obtain pulses from a laser including, Q-switching, gain switching, Kerr-lens mode locking, and mode locking by saturable absorber. Mode locking using saturable absorber is one of the ways in which the shortest pulses can be generated [42]. To have a sense of mode-locked operation, a brief and simplified overview will be presented here. This section is based on the Refs. [41, 43].

Mode-locked operation of a laser occurs by superposition of many monochromatic resonant waves that can be supported by the laser cavity. These longitudinal modes are placed at discrete frequencies given by

$$\nu_q = q\frac{c}{2d} \qquad \text{1-20}$$

where q is an integer, c is the speed of light in vacuum, and d is the effective length of the resonator. Frequency separation between modes is called free spectral range (ν_{FSR}) and given by

$$\nu_{FSR} = \nu_{q+1} - \nu_q = \frac{c}{2d} \qquad \text{1-21}$$

hence, the angular frequency separation between modes is

$$\omega_F = \omega_{q+1} - \omega_q = 2\pi\nu_{FSR} = \frac{\pi c}{d} \qquad \text{1-22}$$

Then the sum of the M oscillating modes in the direction towards the output coupler is given

$$E(t) = \sum_{q=0}^{M-1} E_q \exp\left(i(\omega_0 + q\omega_F)t + i\Phi_q(t)\right) \qquad \text{1-23}$$

where E_q is the amplitude of the qth mode, ω_0 is the angular frequency of the $q = 0$ mode, and $\Phi_q(t)$ is the phase of qth mode. If $\Phi_q(t)$ is constant for all the modes, then the output power ($\propto |E(t)|^2$) will be temporally peaked periodic pulses. In the rest of this calculations, E_q will be taken as the same for each mode to simplify calculations. In reality, however, E_q varies across the gain bandwidth of the gain medium. Taking $E_q = E_0$ and setting $\Phi_q(t) = 0$, Eq. (1-23) can be written as

$$E(t) = E_0 \sum_{q=0}^{M-1} \exp(i(\omega_0 + q\omega_F)t)$$
$$= E_0 \exp(i\omega_0) \frac{1 - \exp(iM\omega_F t)}{1 - \exp(i\omega_F t)}$$
$$= E_0 \frac{\sin\left(\frac{M\omega_F t}{2}\right)}{sin\left(\frac{\omega_F t}{2}\right)} \exp\left[i\left(\omega_0 t + \frac{M-1}{2}\omega_F t\right)\right] \qquad 1\text{-}24$$

Temporal profile of the output power ($\propto |E(t)|^2$) is shown in Figure 1-8 for different number of modes M.

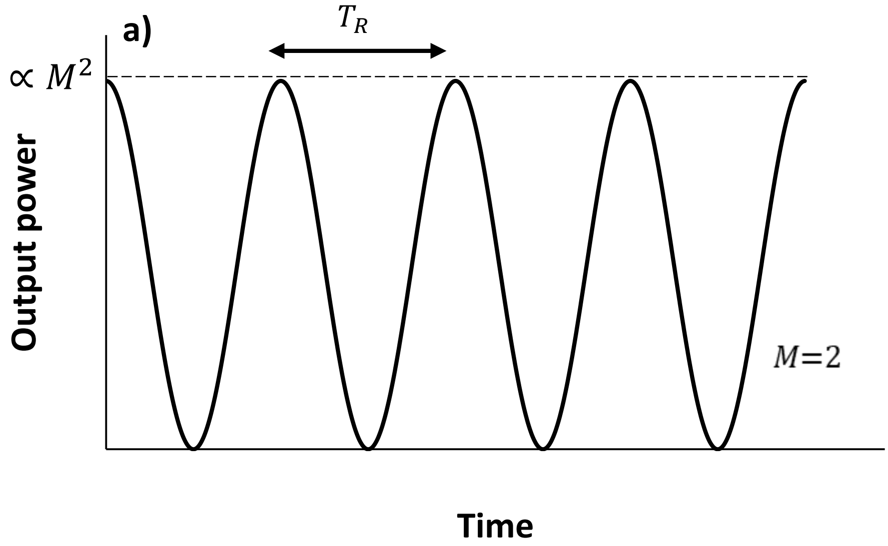

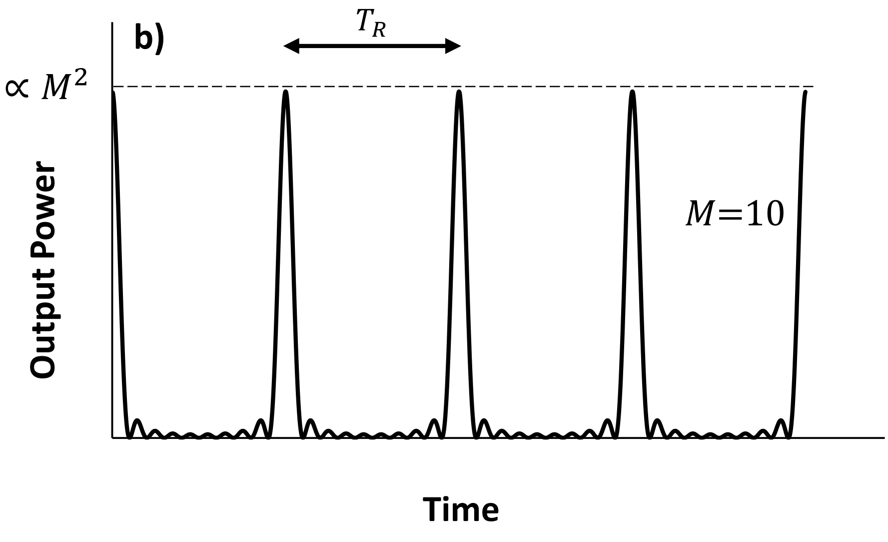

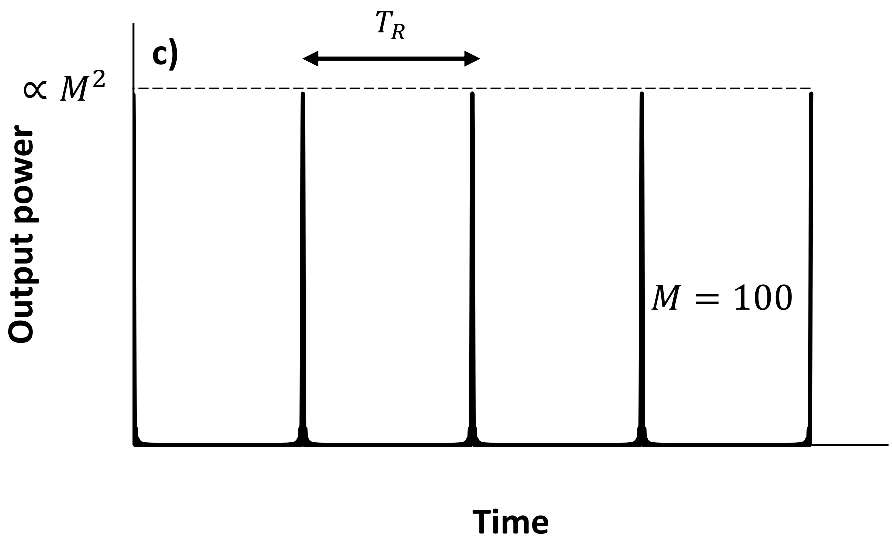

Figure 1-8. Output power of a mode-locked laser as a function of time for the number of locked modes M = (a) 2, (b) 10, (c) 100.

The electric field has a periodicity of $T = 2\pi(2/\omega_F)$, hence the period of the pulses is $T_R = \pi(2/\omega_F) = 2d/c$, which is the cavity round trip time. The maximum amplitude of the electric field can be found from L'Hopital rule as

$$E_{max} = E_0 \left. \frac{cos\left(\frac{M\omega_F t}{2}\right)\frac{M\omega_F}{2}}{cos\left(\frac{\omega_F t}{2}\right)\frac{\omega_F}{2}} \right|_{t=2\pi\left(\frac{2}{\omega_F}\right)} = ME_0 \qquad \text{1-25}$$

From Eq. (1-24), the average output power is proportional to ME_0^2, and the peak average power is, from Eq. (1-25), proportional to $M^2E_0^2$. Therefore, the peak power increases with the number of modes. To determine the pulse width τ_{FW0}, time difference between the pulse peak and the first zero, consider the first zero of the electric field in Eq. (1-24), which is

$$\frac{M\omega_F \tau_{FW0}}{2} = \pi \qquad \text{1-26}$$

leading to the pulse duration of

$$\tau_{FW0} = \frac{1}{M}\frac{2\pi}{\omega_F} = \frac{T_R}{M} \qquad \text{1-27}$$

To find the pulse duration at the full-width half-maximum τ_{FWHM}, consider the series expansion of the square of the expression in Eq. (1.24)

$$\left[\frac{\sin\left(\frac{M\omega_F t}{2}\right)}{sin\left(\frac{\omega_F t}{2}\right)}\right]^2 = M^2 - \frac{\omega_F^2}{12}(M^4 - M^2)t^2 + \cdots \qquad 1\text{-}28$$

For very large M, time from maximum amplitude at $t = 0$ to time at FWHM is given by

$$\frac{\omega_F^2}{12}M^4t^2 = \frac{M^2}{2} \qquad 1\text{-}29$$

Therefore, τ_{FWHM} becomes

$$\tau_{FWHM} = \frac{1}{M}\frac{2\sqrt{6}}{\omega_F} \qquad 1\text{-}30$$

Assuming all the modes in the bandwidth $\Delta\nu$ are mode locked, M is given by $M = \Delta\nu/(c/2d)$. Then the pulse width becomes

$$\tau_{FWHM} \propto \frac{1}{\Delta\nu} \qquad 1\text{-}31$$

For a transform-limited pulse in which all the phase distortions are absent, the product of the bandwidth and the pulse width (FWHM) satisfies the relationship

$$\Delta\nu\tau_{FWHM} = \mathrm{K} \qquad 1\text{-}32$$

where $\mathrm{K} = 0.441$ and 0.315 for a Gaussian and hyperbolic secant-squared ($sech^2$) pulse, respectively.

In usual lasers, the number of mode-locked modes are quite large. Therefore, the summation in Eq. (1-24) can be replaced by an integral

$$E(t) = \int_{-\infty}^{\infty} d\omega\,[E_p(\omega)\exp\big((i\Phi(\omega)\big)\exp(i\omega t)] \qquad 1\text{-}33$$

where $E_p(\omega)$ is the amplitude of the electric field at angular frequency ω and $\Phi(\omega)$ is the phase which should be a constant for a mode-locked operation.

1.6 Pulse Propagation in Dispersive Media

This section is based on [41]. Unlike monochromatic waves which has a definite frequency, pulses are composed of waves with slightly different frequencies. In dispersive media, the refractive index is a function of frequency, hence each wave in the pulse moves with different velocities, resulting a distortion in the spatio-temporal profile of the pulse. The wavenumber $k(\omega)$, in dispersive media, is not a linear function of the angular frequency ω, and can be approximated by Taylor expansion around ω_0 as

$$k(\omega) = k_0 + (\omega - \omega_0)\left.\frac{dk}{d\omega}\right|_{\omega_0} + \frac{1}{2}(\omega - \omega_0)^2\left.\frac{d^2k}{d\omega^2}\right|_{\omega_0} + \cdots \tag{1-34}$$

where ω_0 is the center frequency of the pulse. Also note that the pulse envelope function $\alpha(z,t)$ in dispersive media satisfies the wave equation of

$$\frac{\partial\alpha}{\partial z} = i\frac{k_2}{2}\frac{\partial^2\alpha}{\partial T^2} \tag{1-35}$$

T is defined by the time measured in the reference of the propagating pulse and given by

$$T = t - \frac{z}{u_g} \tag{1-36}$$

where u_g is the group velocity of the pulse. Then it can be shown that a Gaussian pulse with a temporal profile of

$$a(0,T) = a_0 \exp\left(-\alpha T^2\right) \tag{1-37}$$

evolves to a pulse envelope given by the equation

$$a(z,T) = \frac{a_0}{\sqrt{1 + i2\alpha k_2 z}}\exp\left(-\frac{\alpha T^2}{1 + i2\alpha k_2 z}\right) \tag{1-38}$$

at a later position z. For simplicity Eq.(1-35) can be written as

$$a(z,T) = |a(z,T)|\exp\left[i\Phi(z,T)\right] \qquad \text{1-39}$$

It can be shown that the full-width half-maximum (FWHM) duration of the Gaussian pulse at position z is given by

$$T_{1/2}(z) = T_{1/2}\sqrt{1 + \left(\frac{4k_2 z ln(2)}{T_{1/2}^2}\right)^2} \qquad \text{1-40}$$

where $T_{1/2}$ is the FWHM duration of the Gaussian pulse at $z = 0$.

The group delay dispersion having a unit of fs^2 is defined by

$$\begin{aligned} D = \frac{d^2\Phi}{d\omega^2} = l\frac{d^2k}{d\omega^2} = lk_2 = l\frac{d}{d\omega}\frac{1}{u_g} \\ = \frac{d}{d\omega}\left(\frac{l}{u_g}\right) = l\frac{\lambda^3}{2\pi c^2}\frac{d^2n}{d\lambda^2} \end{aligned} \qquad \text{1-41}$$

where l is the length of the medium traversed by the pulse, u_g is the group velocity of the pulse, and k_2 is the second order derivative of the wavenumber $k(\omega)$ with respect to angular frequency. Therefore, Eq. (1-40) can be written using group delay dispersion D as

$$T_{1/2}(z) = T_{1/2}\sqrt{1 + \left(\frac{4D ln(2)}{T_{1/2}^2}\right)^2} \qquad \text{1-42}$$

As said earlier, refractive index dependence of the frequency cause dynamic carrier frequency to vary across the pulse by some amount $\Delta\omega(T)$. For the GDD > 0, the dynamic carrier frequency is downshifted in the leading edge ($T < 0$), and upshifted in the trailing edge ($T > 0$), and it is vice versa when the GDD < 0. Figure 1-9 shows a Gaussian pulse propagating in a nondispersive medium whereas the effect of GDD on the Gaussian pulse is shown in Figure 1-10 and Figure 1-11.

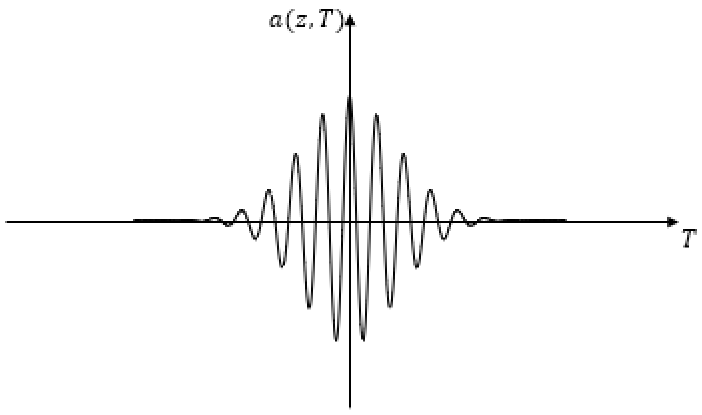

Figure 1-9. Electric field of a Gaussian pulse

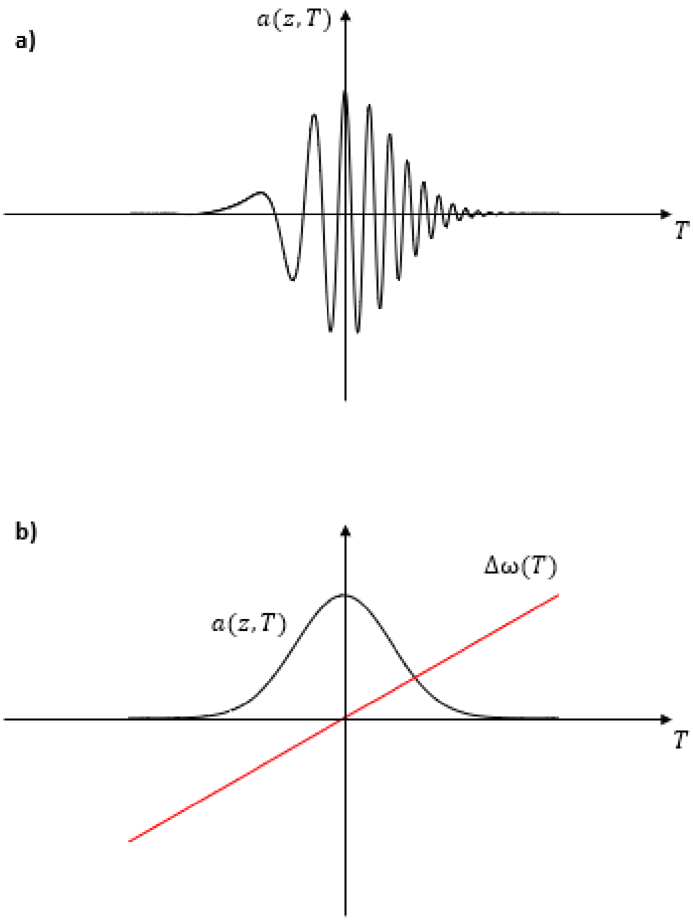

Figure 1-10. (a) Electric field of a Gaussian pulse propagating in a medium where GDD > 0. (b) The change in the dynamic carrier frequency across the Gaussian pulse envelope in a medium where GDD > 0.

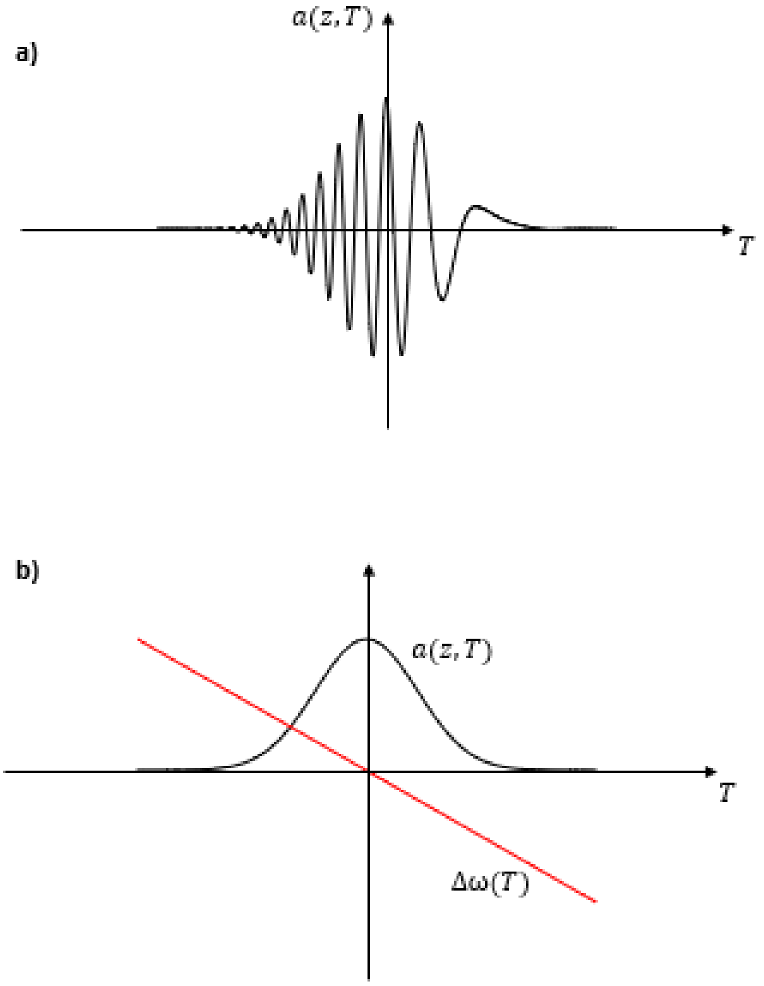

Figure 1-11. (a) Electric field of a Gaussian pulse propagating in a medium where GDD < 0. (b) The change in the dynamic carrier frequency across the Gaussian pulse envelope in a medium where GDD < 0.

1.7 Pulse Duration Measurement Using Interferometric Autocorrelation

Pulse durations down to the order of picoseconds can be measured by using fast photodiodes and oscilloscopes, but these devices are slow to measure femtosecond pulses. In SWCNT-SA mode-locked Cr:LiSAF experiments, where femtosecond pulses were produced, an intensity autocorrelator shown in Figure 1-12 was used to determine the pulse duration. In the interferometric autocorrelator, the input beam was first divided into two equal amplitude beams by the first beam splitter (BS1). These two beams were then superimposed on the second beam splitter (BS2) upon reflection from the corner cube mirrors and sent onto a parabolic mirror. Then, the colinear two beams coming from two arms were focused into a second-harmonic generation crystal (SHG crystal). A lens was placed after the SHG crystal to gather all the beam into the detector. A short-pass filter was used to filter in only the frequency-doubled photons and filter out the pump beam. One of the arm lengths in the interferometric autocorrelator was

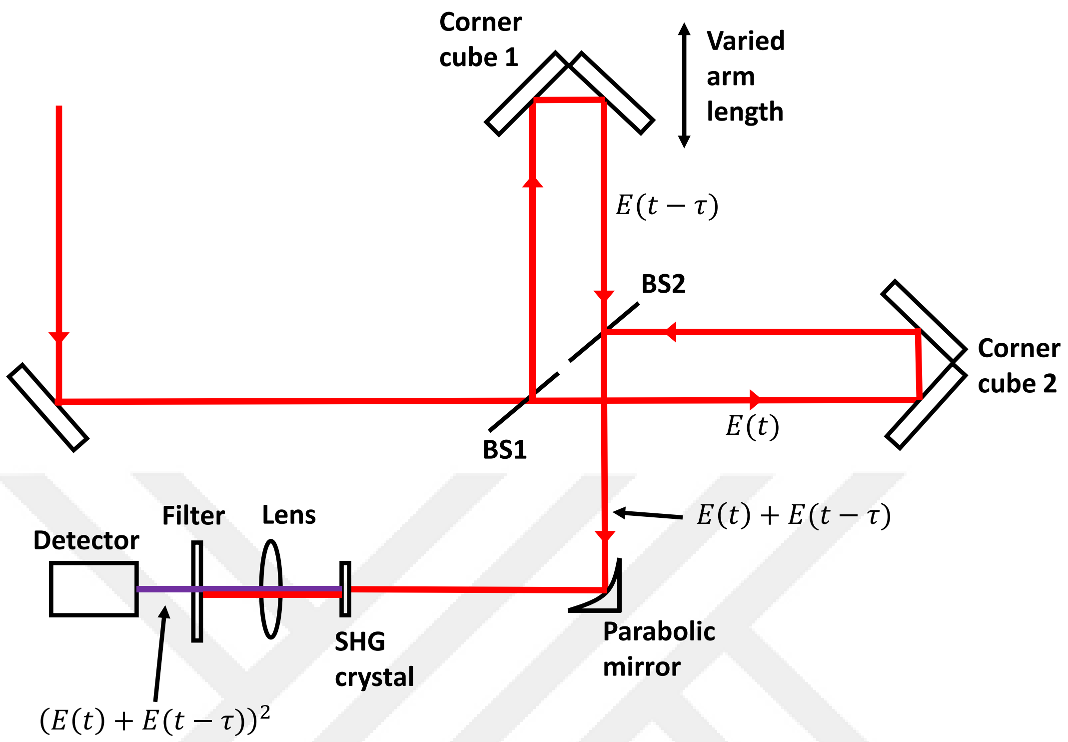

Figure 1-12. Schematic representation of the interferometric autocorrelator used in the SWCNT-SA mode-locked Cr:LiSAF laser experiments.

periodically varied during the measurements so that the pulse in one arm arrives to the BS2 (consequently to the SHG crystal, and the detector) with some delay τ. Therefore, the intensity of the light after SHG crystal is given by

$$I_{AC}(\tau)=\int_{-\infty}^{\infty}\left|\left(E(t)+E(t-\tau)\right)^{2}\right|^{2}dt \quad \text{1-43}$$

Let's examine the two limiting conditions. When the delay $\tau = 0$ Eq. (1-43) becomes

$$I_{AC}(0)=16\int_{-\infty}^{\infty}E^{4}(t)dt \quad \text{1-44}$$

For large delays, Eq. (1-43) becomes

$$I_{AC}(\tau\to\infty)=2\int_{-\infty}^{\infty}E^{4}(t)dt \quad \text{1-45}$$

From Eq. (1-44) and (1-45), it can be clearly seen that the interferometric autocorrelation signal has the well-known ratio of 8:1.

Furthermore, first order interferometric autocorrelation signal is given by

$$g_1(\tau) = \frac{\int_{-\infty}^{\infty} |E(t) + E(t-\tau)|^2 dt}{2\int_{-\infty}^{\infty} |E(t)|^2\, dt} \qquad 1\text{-}46$$

whose Fourier transform is $I(\omega) + I(-\omega)$, hence it only contains information about the spectrum. Pulse duration can be extracted from the second order interferometric autocorrelation signal which is expressed as

$$g_2(\tau) = \frac{\int_{-\infty}^{\infty} \left|\left(E(t) + E(t-\tau)\right)^2\right|^2 dt}{2\int_{-\infty}^{\infty} \left|\left(E(t)\right)^2\right|^2 dt} \qquad 1\text{-}47$$

Second order interferometric autocorrelation signal can be derived for a chirped Gaussian pulse, which has the form

$$E = \frac{1}{2}\exp\left[-(1+ia)(t/\tau_G)^2\right]e^{i\omega_0 t} \qquad 1\text{-}48$$

where ω_0 is the central carrier frequency, $\tau_G = T_{1/2}/\sqrt{2ln2}$ and a is the chirp parameter of the Gaussian pulse. Since the pulse propagates in a dispersive medium, the instantaneous frequency ω of the pulse changes as

$$\omega(t) = \omega_0 + \frac{d}{dt}\Phi(t) \qquad 1\text{-}49$$

Above, $\Phi(t)$ is the phase of the pulse and it is related with a chirped parameter via the following the expression

$$\frac{d}{dt}\Phi(t) = -\frac{2at}{\tau_G^2} \qquad 1\text{-}50$$

Inserting Eq. (1.48) into Eq. (1.47) yields an autocorrelation signal of a chirped Gaussian pulse

$$g_2(\tau) = \left\{1 + 2exp\left[-\left(\frac{\tau}{\tau_G}\right)^2\right] + 4exp\left[-\frac{a^2+3}{4}\left(\frac{\tau}{\tau_G}\right)^2\right]cos\left[\frac{a}{2}\left(\frac{\tau}{\tau_G}\right)^2\right]\cos(\omega_0\tau) + exp\left[-(1+a^2)\left(\frac{\tau}{\tau_G}\right)^2\right]\cos(2\omega_0\tau)\right\} \qquad 1\text{-}51$$

The interferometric autocorrelation signal for an unchirped Gaussian pulse with a duration of 15 fs is given in Figure 1-13. For a linearly chirped Gaussian pulses with different chirped parameters of a the interferometric autocorrelation signals are given in Figure 1-14. Note that although the pulse durations are the same, the autocorrelation signal gets narrower for pulses with increasing degrees of chirp.

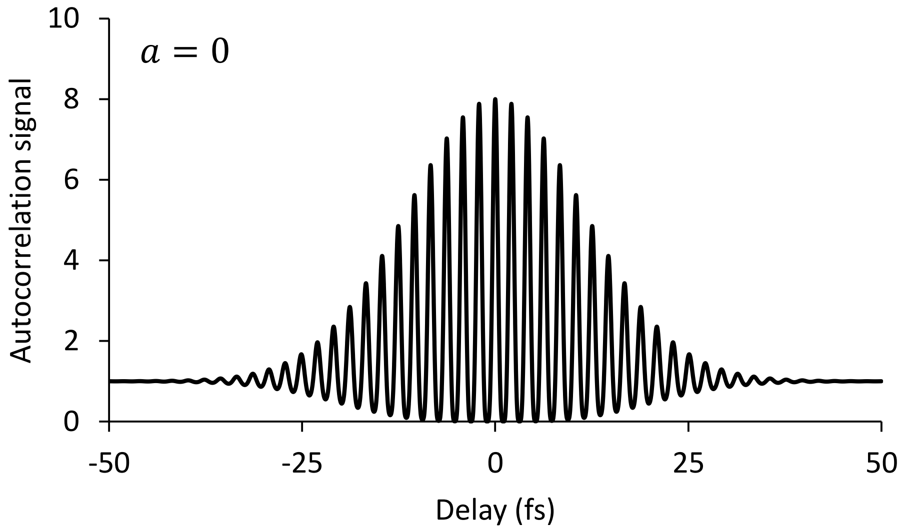

Figure 1-13. Interferometric autocorrelation trace of an unchirped 15-fs Gaussian pulse.

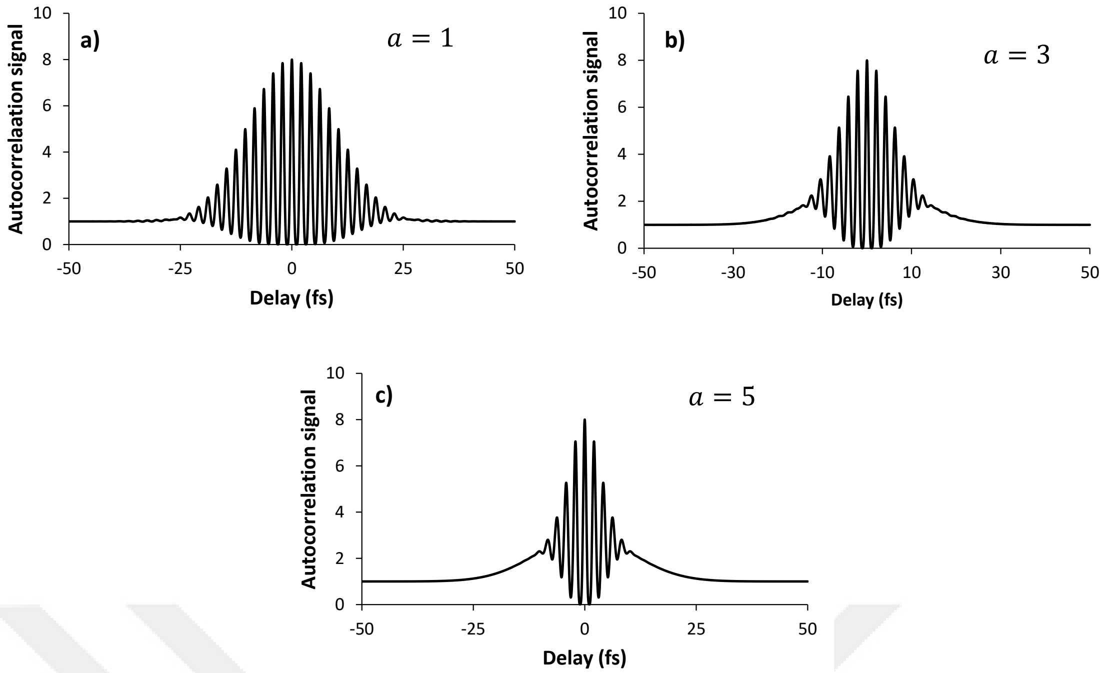

Figure 1-14. Interferometric autocorrelation traces of linearly chirped 15-fs Gaussian pulses with chirp parameters (a) $a = 1$, (b) $a = 3$, (c) $a = 5$. Note the width of the autocorrelator signal shortens as the chirped parameter a increases.

Chapter 2

CONTINUOUS WAVE OPERATION OF A Cr:LiSAF LASER AT 850 nm

2.1 Introduction

In this study, the continuous wave operation of Cr:LiSAF laser at 850 nm was investigated constructing the cavity with different output coupler transmissions. The aim of the experiments was measuring threshold pump power and power efficiency of the laser with different output coupler transmissions. First, the transmission of each output coupler was measured in a systematic way. Then the power efficiency data of the laser with different output couplers were taken. Finally, these are followed by the brief analysis of the data.

2.2. Characterization of the Output Coupler Transmissions

Transmission measurements of the output couplers were conducted with a very small incidence angle since in the actual laser resonator, the output couplers were placed perpendicular to the propagating beam. The incidence angle was not chosen as 0^0 to prevent possible Fabry-Perot effects. To measure output coupler transmissions at 850 nm, a Cr:LiSAF laser working exactly at 850 nm was sent onto the output couplers, as shown in Figure 2-1. The transmission of output couplers was determined by the division of the power of the transmitted beam by the power of the incident beam. To obtain a more reliable data set, the measurement for each output coupler was conducted 10 times.

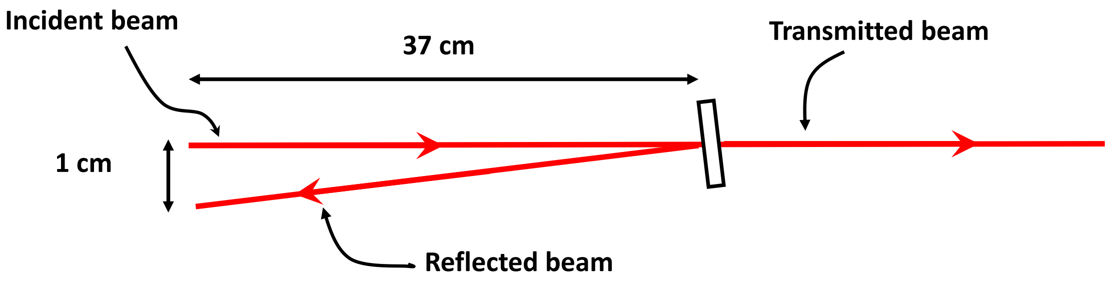

Figure 2-1. Experimental setup used in the measurement of the output coupler transmissions.

The transmission values of the output couplers and their standard errors are summarized in Table 2-1.

Table 2-1. Measured transmission values of the output couplers and their standard errors.

Output Coupler	Transmission (%)	Standard error (%)
OC1	0.13	0.00027
OC2	0.24	0.00051
OC3	0.94	0.0026
OC4	1.85	0.0038
OC5	3.22	0.0072
OC6	4.98	0.028

Given that there is no systematic error introduced to the measurements, very low standard error was an indicator of the reliable data.

2.3 Measurements of the Power Efficiency Curves

Figure 2-2(a) shows the x-cavity Cr:LiSAF laser used to measure the power efficiency curves with output couplers OC1-OC6. To investigate the behaviour of the laser with higher transmission values, OC5 and OC6 were used together in the cavity to have ≈8.2% transmission, as shown in Figure 2-2(b). No lasing was observed with available output couplers having transmission values higher than ≈8.2% at the maximum pump power of 120 mW. Different output couplers forced laser to operate at different wavelengths. This was unwanted because the gain of the laser varies across the spectral range. The problem was overcome by inserting a tuning prism into the cavity and the lasing wavelength was tuned exactly to 850 nm. This guaranteed that the laser gain in each experiment was the same and the only changing parameter during the measurements of power efficiency curves was the transmission of the output couplers.

a)

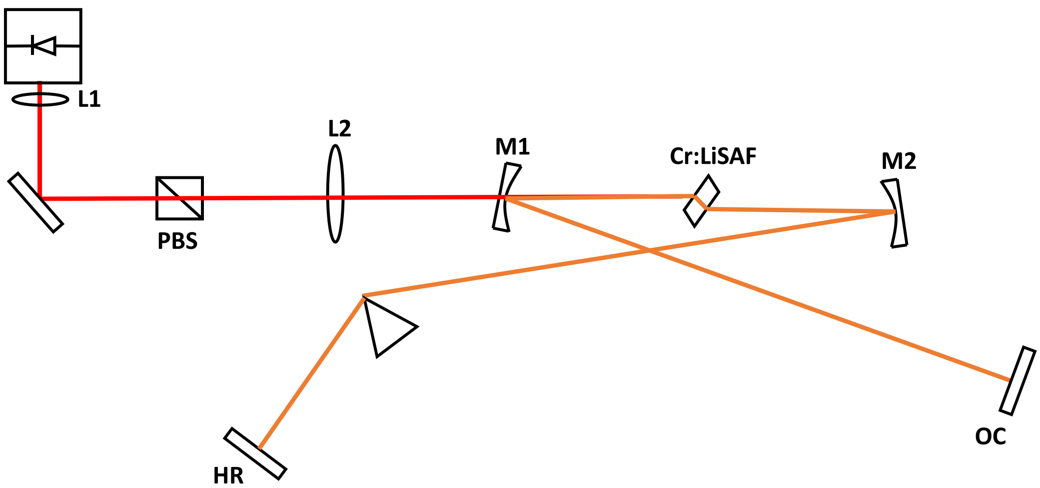

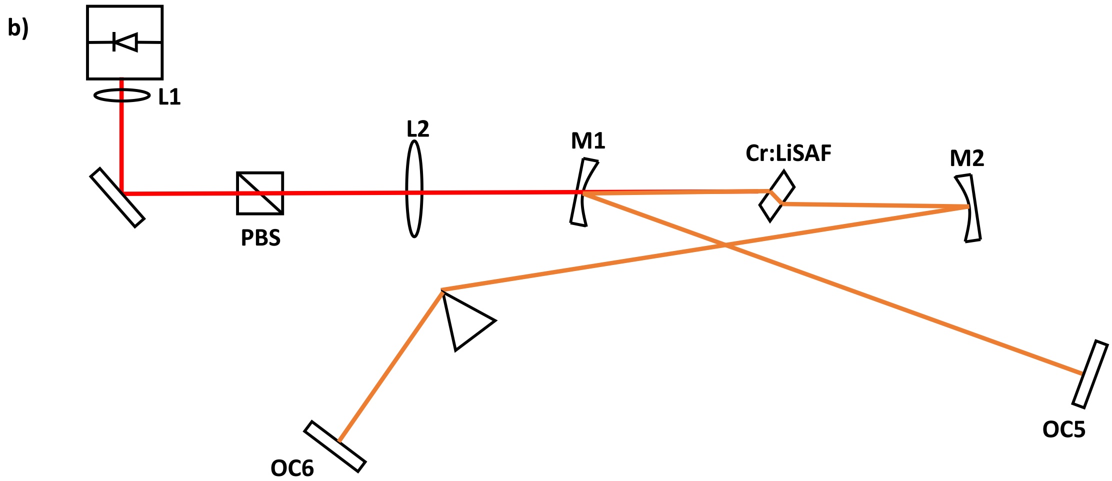

Figure 2-2. (a) Experimental setup of the short x-cavity Cr: LiSAF laser resonator with output couplers OC1-OC6 at 850 nm. (b) Experimental setup of the short x-cavity Cr: LiSAF laser resonator with output couplers OC5 and OC6 at 850 nm.

The efficiency of the laser is defined by the following relation

$$\eta = \frac{P_{in}}{P_{out}} \qquad 2\text{-}1$$

where P_{in} is the pump power measured before lens L2, and P_{out} is the output power of the Cr:LiSAF laser measured right after the output couplers, as shown in Figure 2-2. The power efficiency graphs for each configuration is provided below.

2.2.1 Power efficiency data for 0.13% OC

The laser resonator constructed with this output coupler had a threshold pump power of 6 mW and efficiency of 21%. This output coupler provided the lowest threshold and efficiency values among all the other output couplers.

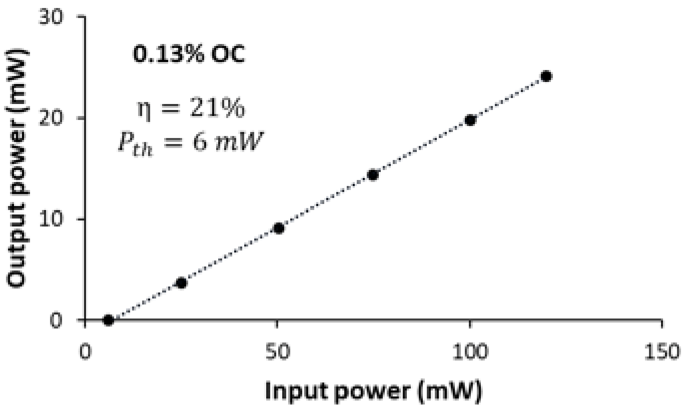

Figure 2-3. Power efficiency of the x-cavity Cr:LiSAF laser at 850 nm taken with 0.13% OC.

2.2.2 Power efficiency data for 0.24% OC

The laser resonator constructed with this output coupler had a threshold pump power of 9 mW and efficiency of 28%.

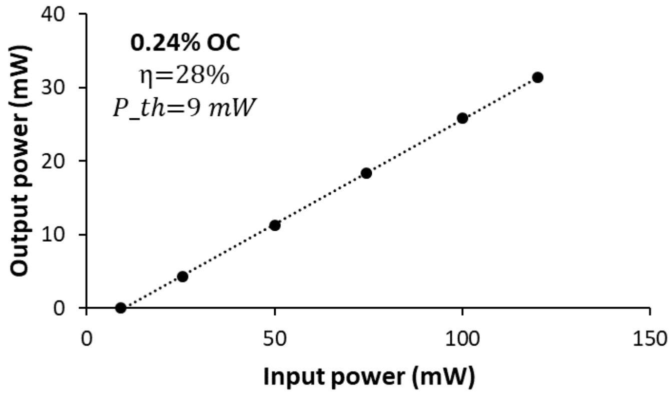

Figure 2-4. Power efficiency of the x-cavity Cr:LiSAF laser at 850 nm taken with 0.24% output coupler.

2.2.3 Power efficiency data for 0.94% OC

The laser resonator constructed with OC3 had a threshold pump power of 16 mW. The efficiency of the laser with this configuration was 48%, which is quite close to 50%, the maximum efficiency reached in our experiments.

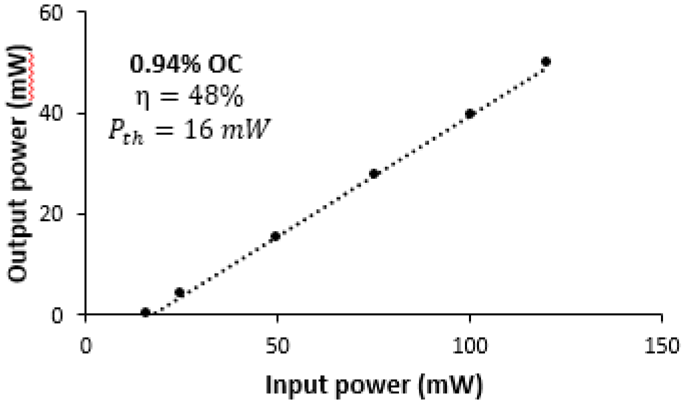

Figure 2-5. Power efficiency of the x-cavity Cr:LiSAF laser at 850 nm taken with 0.94% OC.

2.2.4 Power efficiency data for 1.85% OC

The laser resonator constructed with this output coupler had a threshold pump power of 33.8 mW. The efficiency of laser with this configuration was 47%, quite close to the maximum efficiency of 50%.

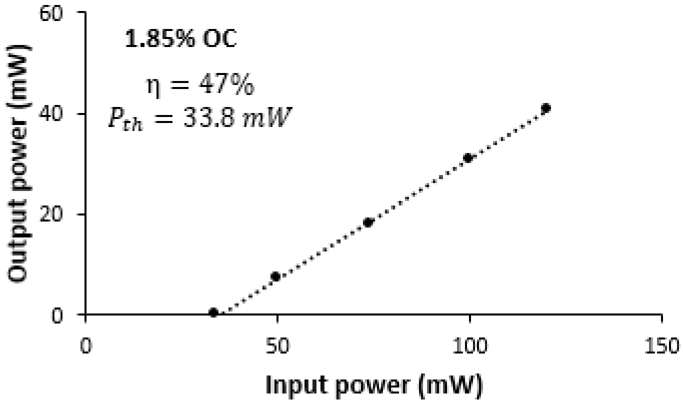

Figure 2-6. Power efficiency of the x-cavity Cr:LiSAF laser at 850 nm taken with 1.85% OC.

2.2.5 Power efficiency data for 3.22% OC

The laser resonator constructed with OC5 had a threshold pump power of 32.7 mW and efficiency of 50%. This efficiency, which is very close to the intrinsic efficiency of Cr:LiSAF lasers [44], also represents the maximum efficiency obtained in our experiments with different output couplers.

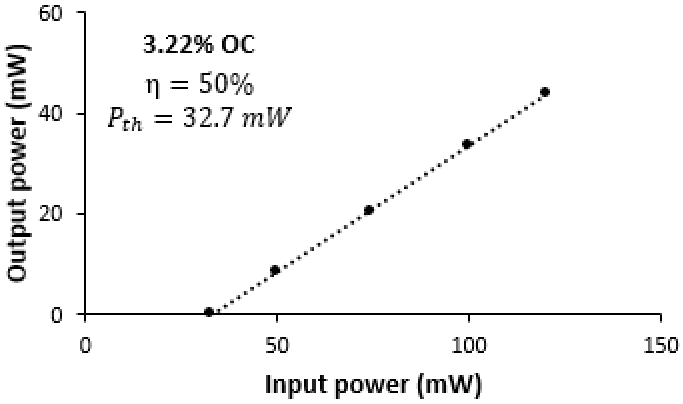

Figure 2-7. Power efficiency of the x-cavity Cr:LiSAF laser at 850 nm taken with 3.22% OC.

2.2.6 Power efficiency data for 4.98% OC

The laser resonator constructed with this output coupler had a threshold pump power of 60 mW. The efficiency of the laser with this configuration was also 48%, quite close to the maximum efficiency of 50%.

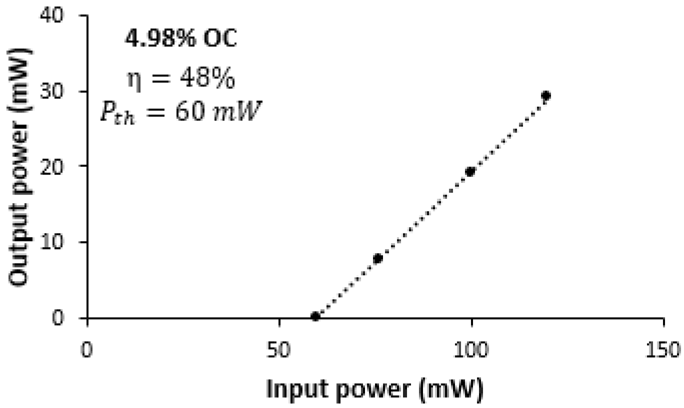

Figure 2-8. Power efficiency of the x-cavity Cr:LiSAF laser at 850 nm taken with 4.98% OC.

2.2.6 Power efficiency data for 3.22% + 4.98% = 8.2% OC

The sum of the transmissions of these two output couplers was 8.2%. The laser resonator constructed with both output couplers together, as shown in Figure 2-2(b), had a high threshold pump power of 108 mW and efficiency of 44%.

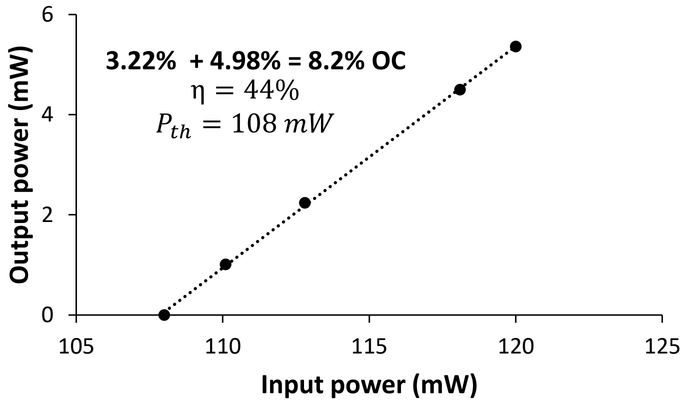

Figure 2-9. Power efficiency of the x-cavity Cr:LiSAF laser at 850 nm taken with 3.22% + 4.98% = 8% OC.

From Eq. (1-18), it is expected a linear relation between the transmission of the output coupler and pump threshold power, as shown in Figure 2-10. Dividing the intercept by the slope of the line, the loss of the x-cavity Cr:LiSAF laser is found to be 0.35%.

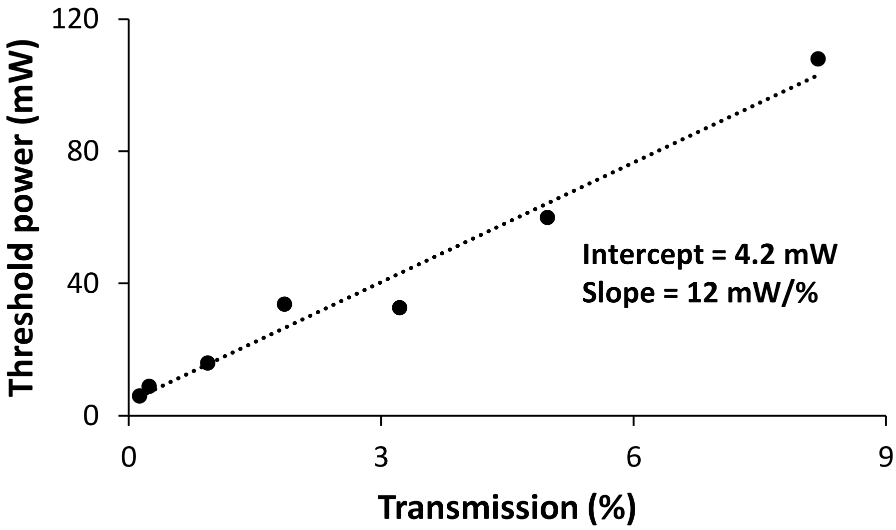

Figure 2-10. Threshold pump power of x-cavity Cr:LiSAF laser at 850 nm as a function of output coupler transmission.

Other useful relations to fully characterize the four-level laser systems like Cr:LiSAF are the measurements of η and $P_{th}\eta/T$ as a function of the output coupler transmission. These relations can reveal the possible power degrading mechanisms present in some four-level laser systems [45]. Figure 2-11 shows the relation between the output coupler transmission and the efficiency of the x-cavity Cr:LiSAF laser at 850 nm. The efficiency of the laser increases with increasing transmission values of the output couplers at first and then decreases slowly until the maximum transmission value of 8.2%.

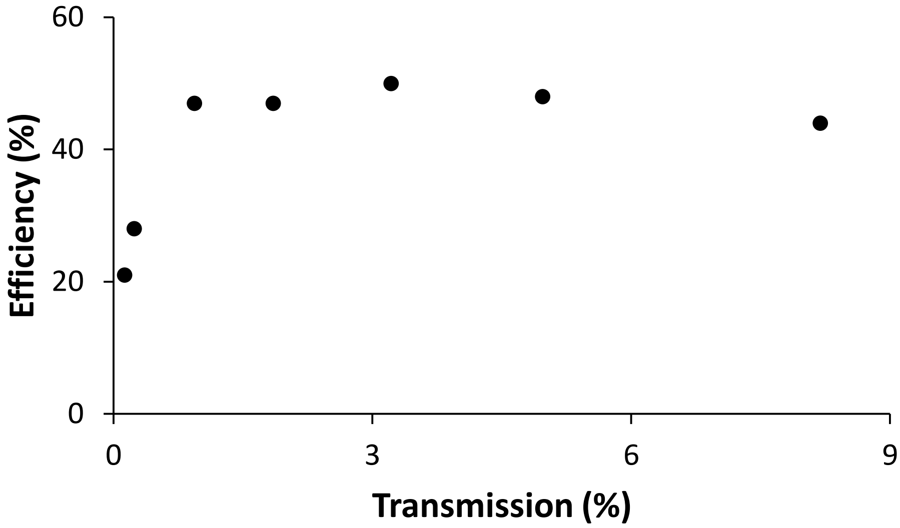

Figure 2-11. Efficiency of the x-cavity Cr:LiSAF laser at 850 nm as a function of the output coupler transmission.

The relation between the expression $P_{th}\eta/T$ and output coupler transmission is given in Figure 2-12. The expression $P_{th}\eta/T$ is a constant function of output coupler transmission for ideal four-level lasers. In the experimental data however, $P_{th}\eta/T$ decreases at first and then reaches a steady value at high output coupler transmissions. This may be due to an error in the transmission measurements of output couplers with low transmission or there may be power-degrading mechanisms involved in the operation of Cr:LiSAF lasers. This point requires further examination.

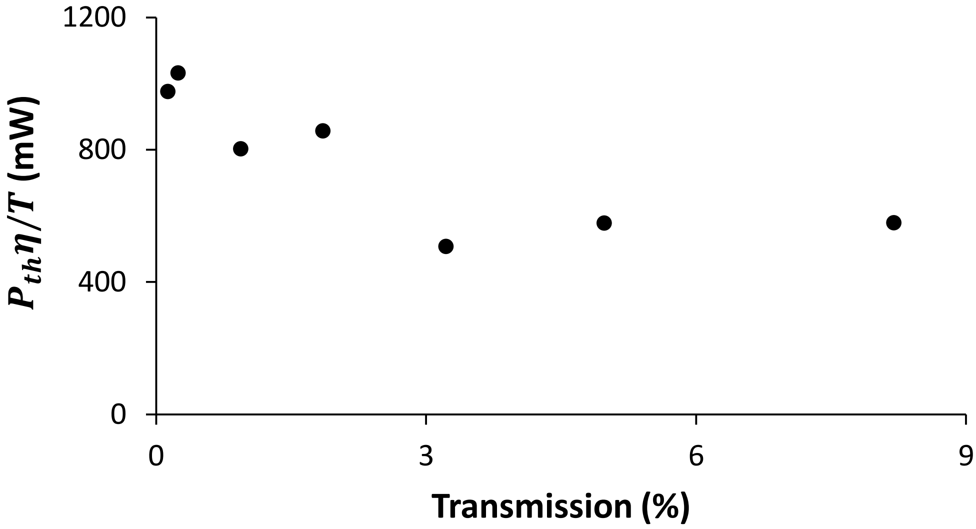

Figure 2-12. $P_{th}\eta/T$ vs output coupler transmission for the x-cavity Cr:LiSAF laser at 850 nm.

For a four-level laser, $P_{th}\eta/T$ can be expressed in terms of the saturation power [See Eq. (1-11)] using the formula found in Ref. [45].

$$\frac{P_{th}\eta}{T} = \frac{P_{sL}}{2} = \frac{h\nu_L}{2\sigma_e\tau_f}a_L \quad \text{2-2}$$

Inserting the average of measured $P_{th}\eta/T$ values which came to be 0.762 W and the calculated root mean square of the laser beam radius $w_L = 20\ \mu m$ into Eq. (2.2), emission cross section - fluorescence lifetime product is determined to be 385×10^{-20} cm^2 - μs, which is in fair agreement with 322×10^{-20} cm^2 - μs reported in the literature [24].

2.4 Conclusions

In this chapter, a detailed experimental characterization of the Cr:LiSAF laser was presented. Output couplers with different transmissions were used to measure the power efficiency of the laser. Slope efficiency of 50% in the best case was achieved and this was quite close to the intrinsic slope efficiency of the Cr: LiSAF lasers [44]. Finally, emission cross section - fluorescence lifetime product was determined to be similar with the value in literature using all the experimental data.

Chapter 3
Single-Walled Carbon Nanotube Saturable Absorber Mode-Locked Cr:LiSAF Laser Generating 21-fs Pulses at 850 nm

In this study, the direct generation of the shortest pulses (21 fs) from a SWCNT-SA mode locked solid-state laser was achieved. In the experiments, diode-pumped Cr:LiSAF laser was used with an extended resonator to scale up the pulse energy. At pump power levels as low as 210 mW, 21 fs pulses could be generated at a pulse repetition rate of 47.9 MHz and pulse peak power of 9 kW. The origin of the second peak at 899 nm in the optical spectrum of the pulses was investigated and attributed to the Raman generation inside the Cr:LiSAF crystal. It was also verified that the SWCNT-SA used in this experiment was not a limiting factor in obtaining shorter pulses. Ultrafast pump–probe measurements were further carried out to determine the modulation depth, relaxation times, and saturation fluence of the SWCNT-SA used in the experiments.

The transmission-type SWCNT-SA was fabricated by using the SWCNTs synthesized via the high-pressure CO conversion technique (HiPCO) as described in [32]. The linear and nonlinear optical characteristics of the SWCNT-SA are summarized in Figure 3-1.

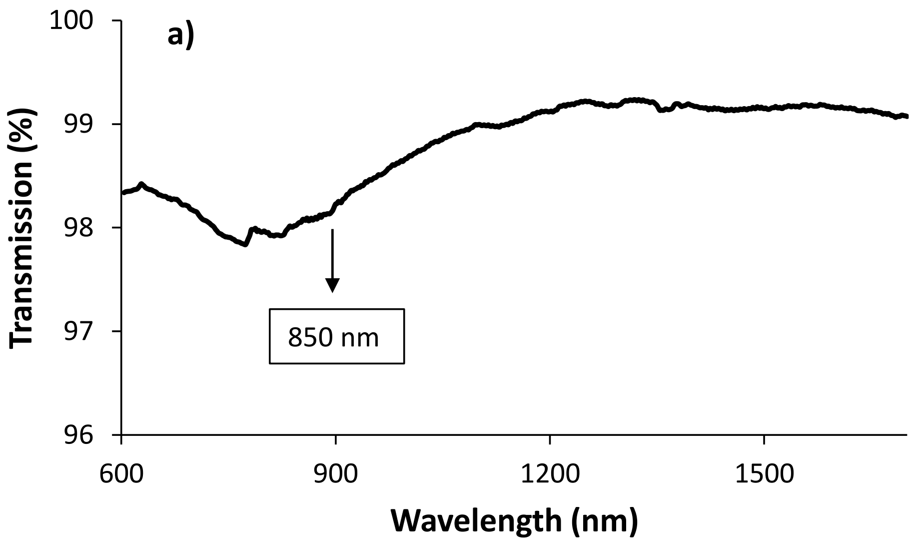

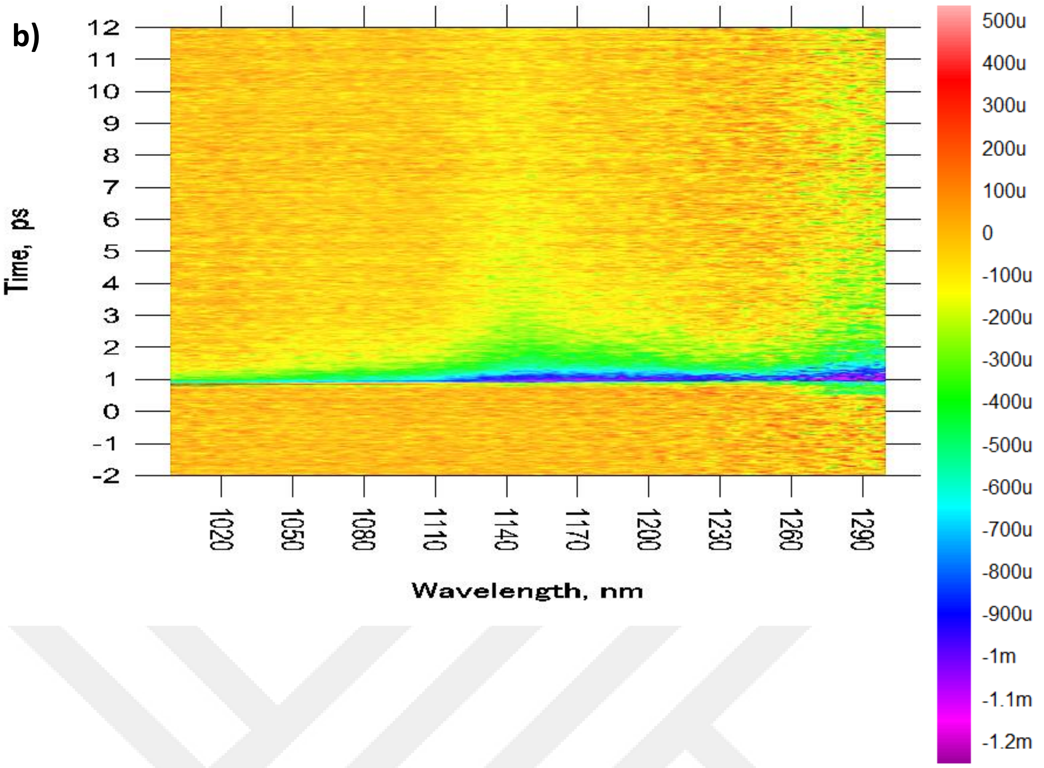
b)
Time, ps
12
11
10
9
8
7
6
5
4
3
2
1
0
-1
-2
1020
1050
1080
1110
1140
1170
1200
1230
1260
1290
Wavelength, nm
500u
400u
300u
200u
100u
0
-100u
-200u
-300u
-400u
-500u
-600u
-700u
-800u
-900u
-1m
-1.1m
-1.2m

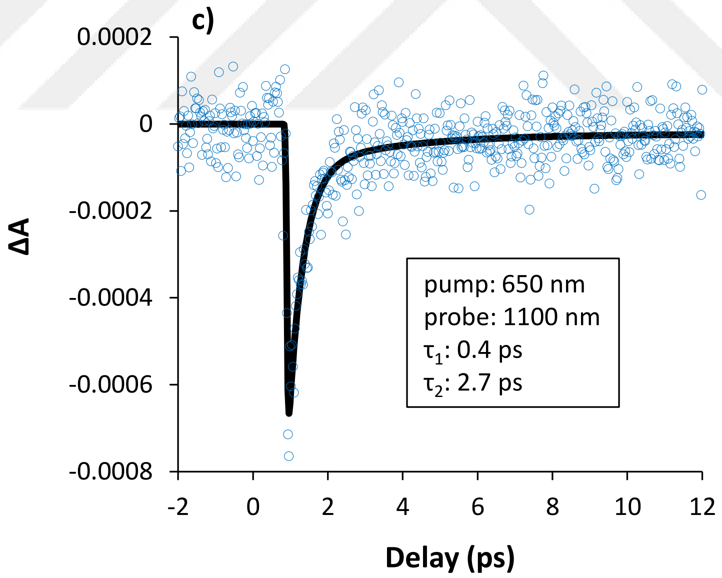
c)
0.0002
0
-0.0002
-0.0004
-0.0006
-0.0008
ΔA
-2
0
2
4
6
8
10
12
Delay (ps)
pump: 650 nm
probe: 1100 nm
τ1: 0.4 ps
τ2: 2.7 ps

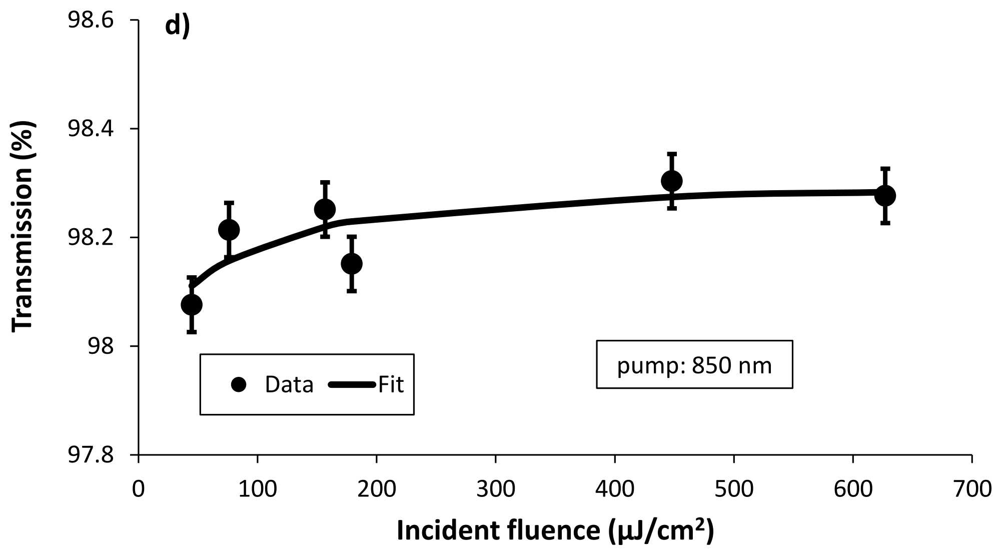

Figure 3-1. (a) Measured steady-state transmission spectrum of the SWCNT-SA. (b) ΔA surface plot of the SWCNT-SA as a function of the nearinfrared continuum probe wavelength and probe delay. (c) A representative time-resolved response of the SWCNT-SA measured at the probe wavelength of 1100 nm. (d) Measured variation of the average transmission of the SWCNT-SA as a function of the incident fluence at 850 nm.

The measured substrate corrected single-pass linear transmission was about 98% at 850 nm [Figure 3-1(a)]. In the pump–probe experiments, an optical parametric amplifier (OPA, TOPAS Prime, pumped at 800 nm by a 1 kHz, 100 fs Ti:sapphire regenerative amplifier, Spitfire Ace, Spectra Physics) was used to pump the SWCNT-SA at 650 nm. The nonlinear absorbance ΔA (ΔA = pumped absorbance– unpumped absorbance) as well as the ultrafast decay times of the SWCNT-SA were measured with femtosecond near-infrared continuum probe pulses. The probe spectrum was kept within the 1000–1240 nm wavelength range to maintain a sufficiently high signal-to-noise ratio during the experiments. The pump wavelength (650 nm) overlapped well with the 850 nm band of the SWCNT-SA and remained sufficiently far from the probe wavelengths to eliminate noise originating from scattered pump light. As can be seen from Figure 3-1(b), the SWCNT-SA exhibited saturable absorption ($\Delta A < 0$) with ultrafast relaxation times on the order of a few ps over a broad wavelength range from 1000 to 1240 nm, in good agreement with previous measurements [32]. Figure 3-1(c) further shows a sample transient absorbance measurement at the probe wavelength of 1100 nm, where a biexponential fit was used, yielding fast and slow relaxation times of 0.4 ps and 2.7 ps, respectively [32]. Biexponential fits performed at the other probe wavelengths (1050, 1150, and 1200 nm) showed that the measured slow (fast) components of the relaxation were in the range of 0.8–2.7 ps (0.1–0.4 ps). Finally, Figure 3-1(d) shows the measured nonlinear transmission of the SWCNT-SA as a function of the incident fluence at 850 nm. Here, the 850 nm output of the OPA was used as the pump, and the nonlinear transmission of the sample was averaged over the 1150–1250 nm wavelength range, where the signal noise was relatively low. The saturation fluence and single-pass modulation depth of the SWCNT-SA were determined as 45 μJ/cm^2 and 0.3% at the pump wavelength of 850 nm by using the method described in [46]. Furthermore, the average diameter of the SWCNTs distributed in the absorber layer was estimated to be in the range between 0.8 and 1.2 nm, in agreement with our previous study [32]. The saturation parameters (relaxation time, saturation fluence, and modulation depth) of the SWCNT-SA used in this study were suitable for the initiation of mode-locked pulse generation from the low-gain Cr:LiSAF laser.

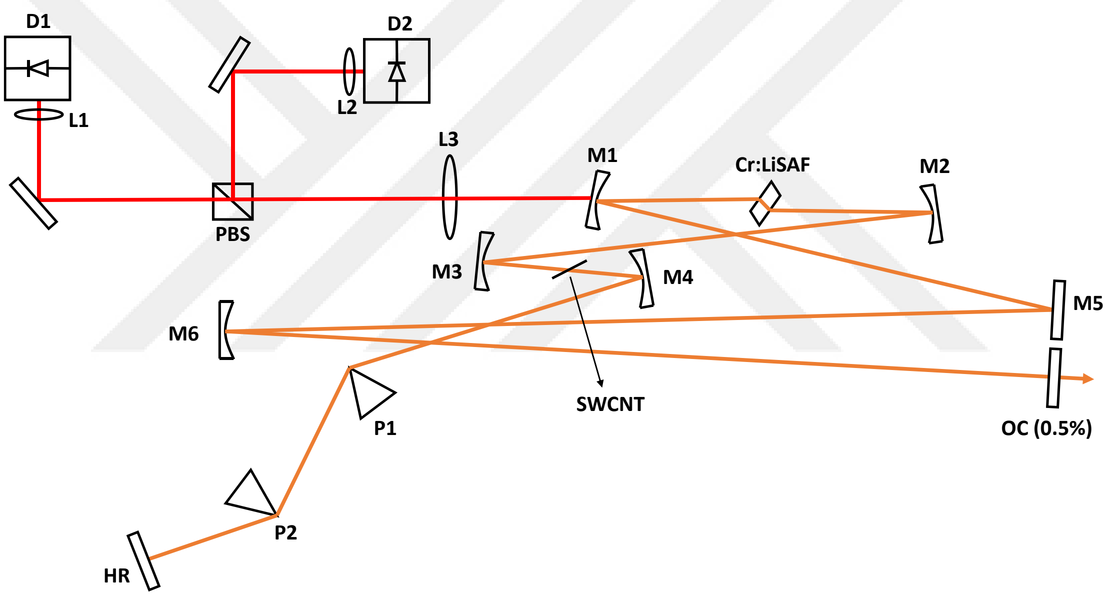

Figure 3-2. Experimental setup of the SWCNT-SA mode-locked Cr: LiSAF laser resonator.

Figure 3-2 shows the schematic of the SWCNT-SA mode locked Cr:LiSAF laser resonator. In the experiments, the Cr:LiSAF gain medium was pumped with two single-mode, 660 nm diode lasers (D1 and D2). One of the diodes had an integrated, internal beam correcting optics. Output beams of the two pump diodes were collimated with aspherical lenses (L1 and L2; f = 4.5 mm) and combined by using a polarizing beam splitter (PBS). The diode beams were then focused inside a Brewster-cut, 8-mm-long Cr:LiSAF crystal (1.5% chromium-doped; pump absorption = 98.5% at 660 nm) by using a focusing lens (L3; f = 6 cm). As shown in Figure 3-2, the Cr:LiSAF crystal was placed between the two curved mirrors (M1 and M2) each with radius of curvature (ROC) of 7.5

cm. Pump and laser spot sizes inside the Cr:LiSAF crystal were estimated to be 16 μm and 18 μm, respectively. A pair of curved mirrors (M3 and M4; ROC = 7.5 cm) was further used to effectively saturate the SWCNT-SA. In addition to the negative GDD introduced by the cavity mirrors (M1, M2, M3, M4, M5, M6, and HR), a pair of fused silica prisms (P1 and P2) was also placed in the high reflector (HR) arm of the resonator for fine adjustment of the cavity GDD. In order to further increase the intracavity pulse energies, the resonator length was increased, extending the output coupler arm with a curved mirror (M6; ROC = 1 m). Hence, the total round trip length of the resonator (Figure 3-2) became 622 cm, corresponding to a pulse repetition rate of 47.9 MHz.

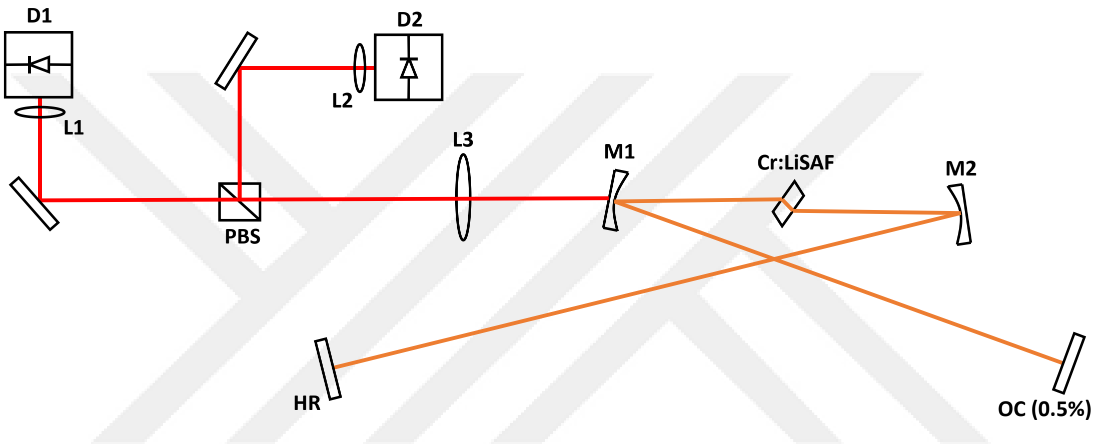

Figure 3-3. Experimental setup of the short x-cavity Cr: LiSAF laser resonator.

Figure 3-4 shows the continuous-wave power efficiency curves of the short x-cavity (round trip length = 203 cm, Figure 3-3) Cr:LiSAF laser with five different output couplers. Based on the measured threshold pump power data, the round trip passive loss of the short x-cavity was estimated to be 0.31%.

As previously mentioned, the short x-cavity was extended to increase the intracavity energy of the laser during mode-locked operation. The mode-locking experiments were conducted with the 0.5% OC, since it provided high intracavity energy as well as high power efficiency. Figure 3-5 further shows the continuous-wave efficiency curves of the extended resonator containing a bare fused silica substrate and a SWCNT-SA on fused silica. The measured incident threshold pump power of the x-cavity increased from 10.4 mW to 12 mW, after the insertion of two prisms, fused silica without SWCNT-SA, and mirrors M3–M6, corresponding to an additional round trip cavity loss of 0.16%. Insertion of the SWCNT-SA further increased the threshold pump power to 53 mW. The round trip cavity insertion loss due to the SWCNT-SA was estimated to be 3.3%.

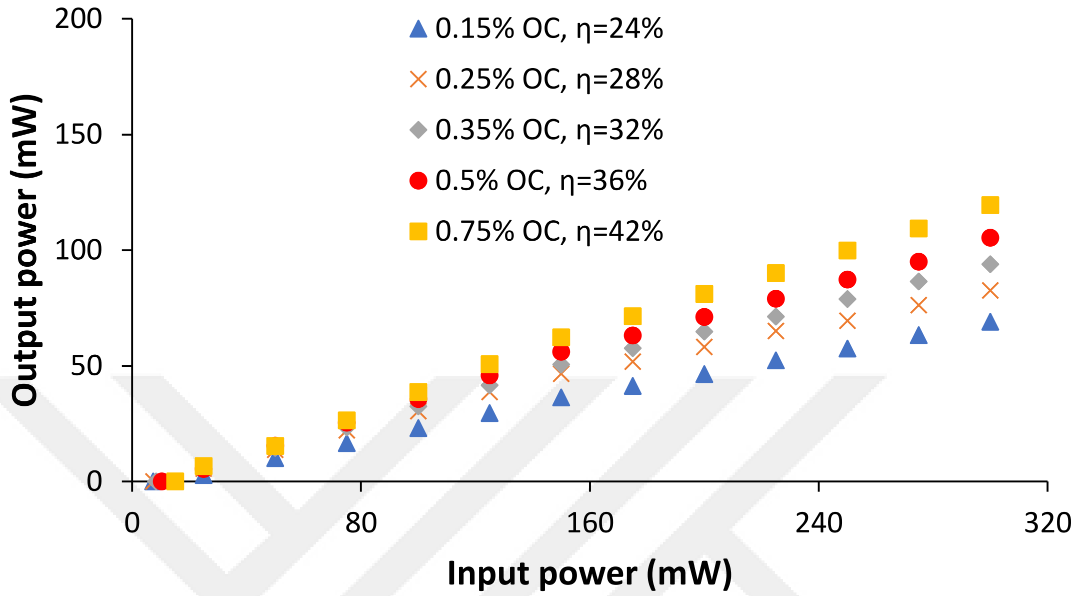

Figure 3-4. Continuous-wave power efficiency curves of the short x-cavity Cr:LiSAF laser operated with five different output couplers.

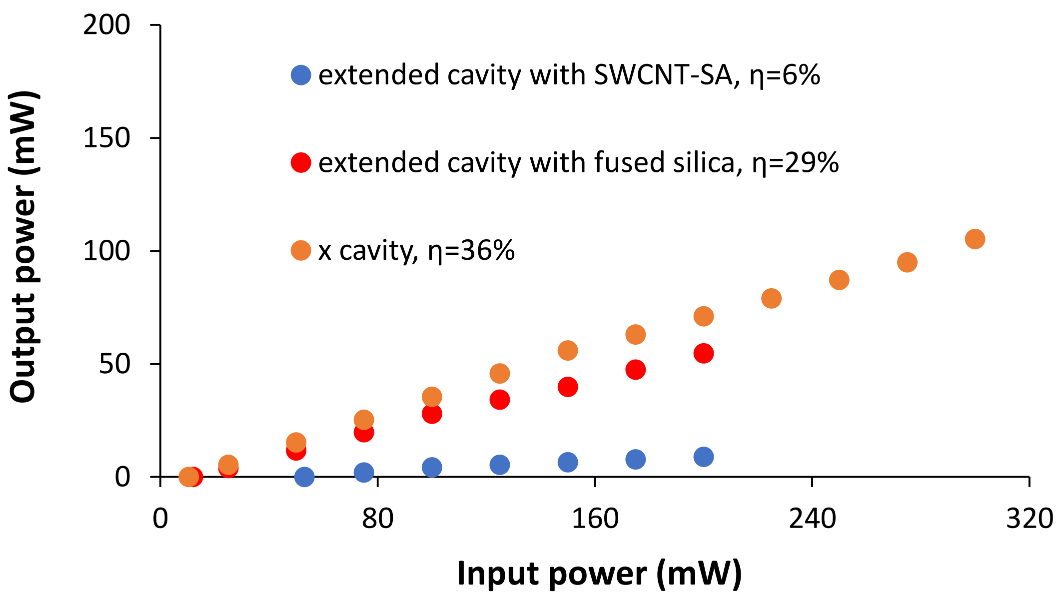

Figure 3-5. Measured continuous-wave power efficiencies of the composite resonator containing a bare fused silica substrate and SWCNT-SA on fused silica.

After the insertion of the SWCNT-SA, mode locking could be initiated by translating the output coupler of the Cr:LiSAF laser. The output characteristics of the mode-locked pulses are summarized in Figure 3-6.

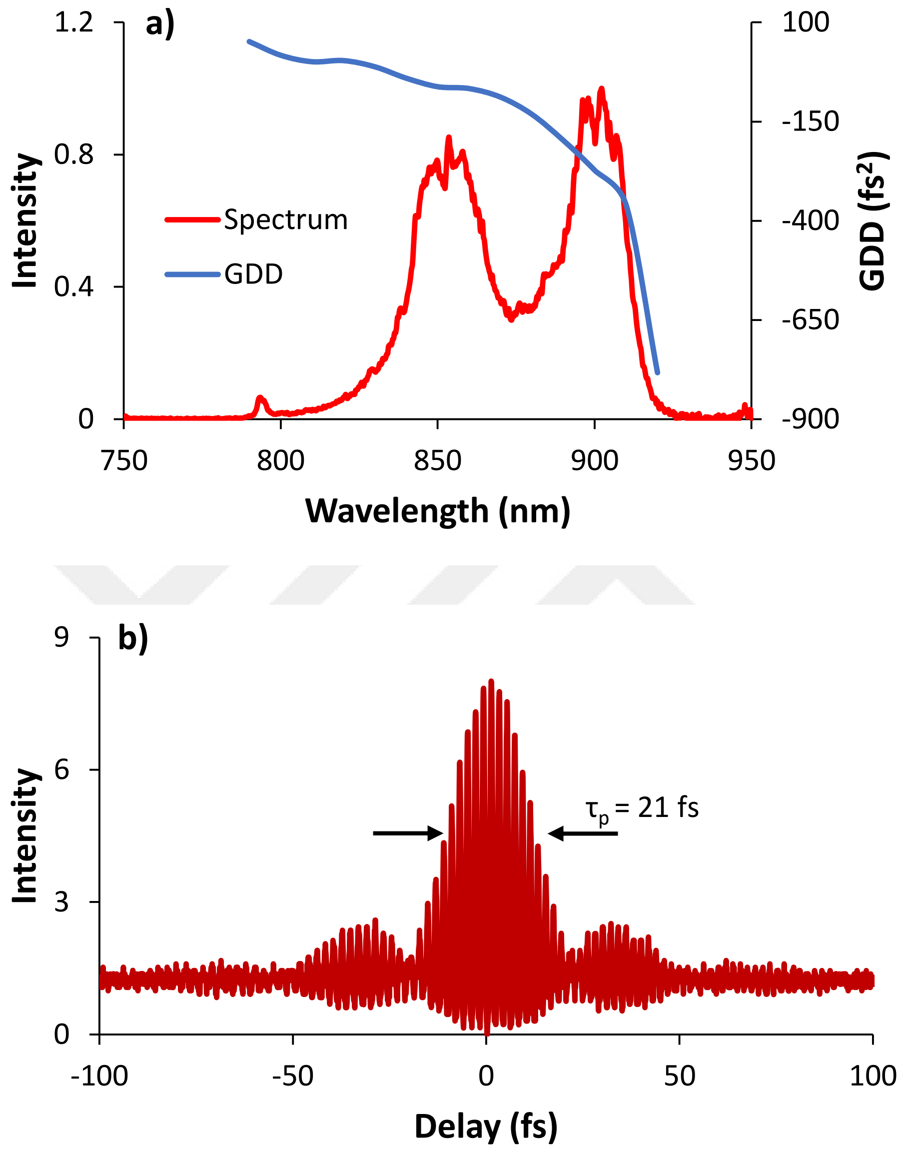

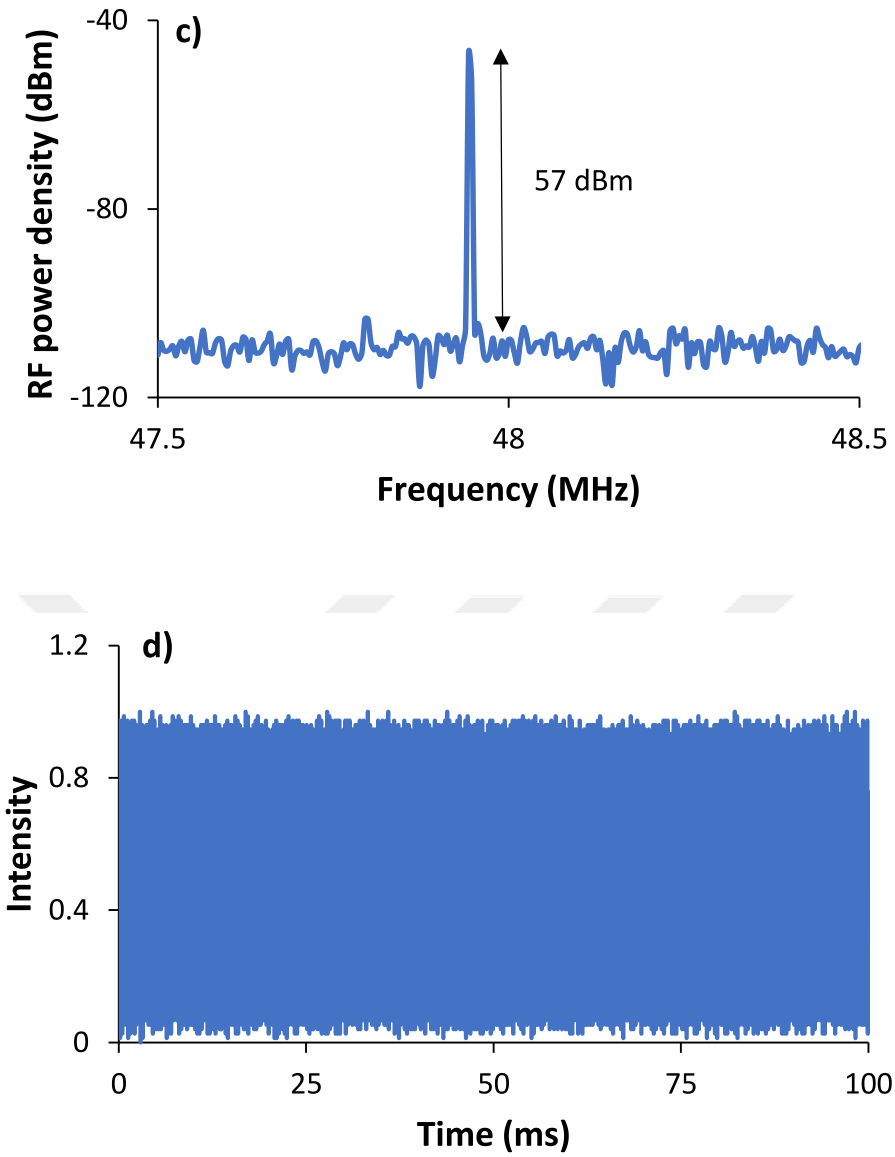

Figure 3-6. (a) Measured mode-locked spectrum of the 21 fs pulses and estimated round trip GDD of the resonator as a function of wavelength. (b) Interferometric autocorrelation trace of the 21 fs pulses. (c) Radio frequency (RF) spectrum of the 47.9 MHz pulse train measured with a resolution bandwidth of 1 kHz. (d) Measured mode-locked pulse train over ms time scales, showing no Q-switching instabilities.

To obtain the shortest pulses, the total GDD of the resonator was controlled by varying the prism separation and insertion. Figure 3-6(a) shows the estimated total GDD of the SWCNT-SA mode-locked Cr:LiSAF laser as a function of wavelength due to the Cr:LiSAF gain medium (23 fs^2 per mm at 850 nm), fused silica prism pair (tip-to-tip separation = 30.1 cm), fused silica substrate insertion (39 fs^2 per mm at 850 nm), air (20 fs^2 per meter at 850 nm), and the dispersion control mirrors (M1, M2, M3, M4, M5, M6, HR). The net estimated round trip GDD came to −62 fs^2 near 850 nm. Figure 3-6(a) further shows the measured mode-locked spectrum of the 21 fs Cr:LiSAF laser. Note that the sharp increase of the negative GDD due to the resonator mirrors beyond 920 nm prevented further spectral broadening of the pulses on the long-wavelength side. This sharp increase of the negative GDD due to the contributions only from resonator mirrors can be seen in Figure 3-7.

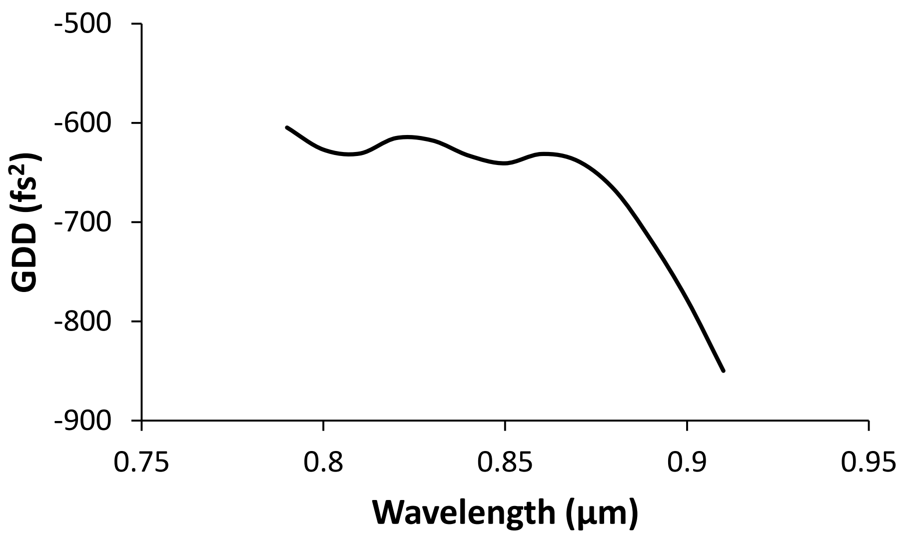

Figure 3-7. Net GDD curve as a function of wavelength due to the resonator mirrors, excluding air, the prisms, crystal, and SWCNT-substrate.

In addition, the spectrum of the pulses deviated from that of an ideal $sech^2$ pulse because of the second peak at 899 nm. This is mainly because the dominant Raman shift in the Cr:LiSAF medium occurs at 561 cm^{-1} [19], shifting the fundamental peak near 854 nm to 896 nm. To verify this the cavity dispersion was slightly increased by adjusting the prism insertion to broaden the pulse duration to about 25 fs, as shown in Figure 3-8. At this setting, an increase in the peak at 899 nm was observed with the increasing pump power.

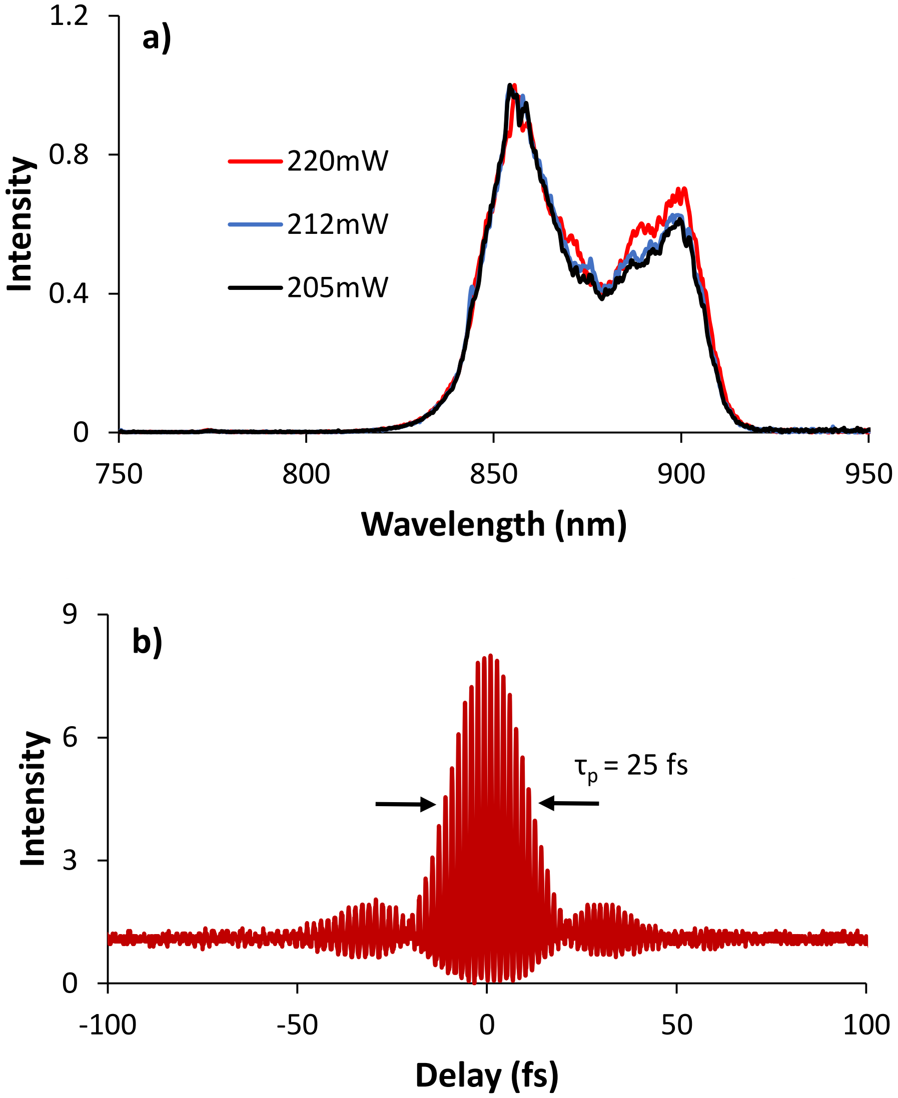

Figure 3-8. Measured spectrum of the pulses at different pump powers (a), when the pulse width was around 25 fs (b).

The same experiment was repeated after optimizing the cavity dispersion to achieve the shortest pulses of 21 fs. In this case, saturation in the pulse energy was observed, hence the output power of the laser remained nearly the same as a function of pump power in the range of 195-220 mW. As a result, the pulse spectrum did not vary with the pump power in this case. The data are shown in Figure 3-9.

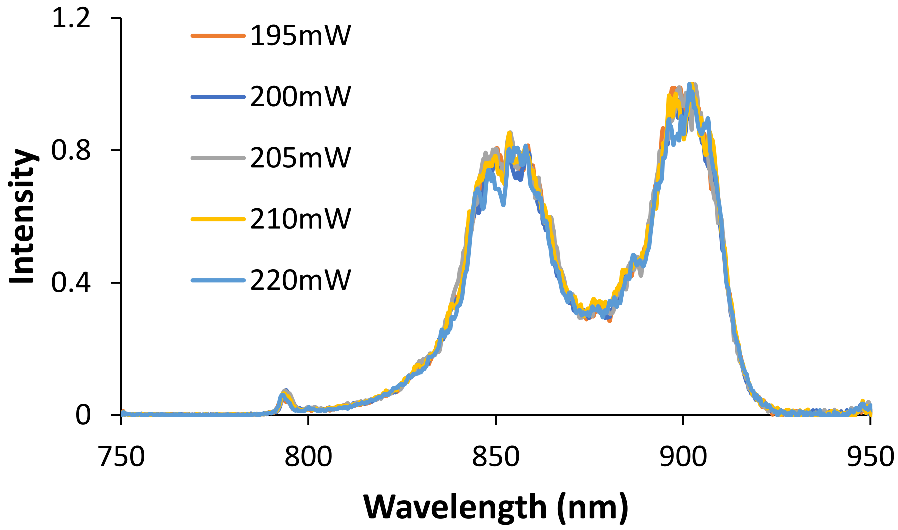

Figure 3-9. Measured spectrum of the pulses at different pump powers, when the pulse width was around 21 fs.

The transform-limited pulse width, based on the measured spectrum of the pulses [Figure 3-6(a)], was calculated to be 15 fs with a time-bandwidth product of 0.40 and autocorrelation conversion factor of 1.53. The actual pulse duration measured from the interferometric autocorrelation [Figure 3-6(b)] came to 21 fs, with a time-bandwidth product of 0.56, indicating that the generated pulses were slightly chirped.

The measured radio frequency (RF) spectrum [Figure 3-6(c)] of the pulse train had a peak centered at 47.9 MHz with a contrast of 57 dB above the noise floor. Furthermore, as can be seen from the pulse train measured over ms time scales [Figure 3-6(d)], the mode-locked operation was free from Q-switching instabilities. At the pump power of 210 mW, the output power of the mode-locked Cr:LiSAF laser was 8.6 mW with a corresponding pulse energy and pulse peak power of 0.18 nJ and 9 kW, respectively. For the calculated beam waist of 21 μm, the incident fluence on the SWCNT-SA was estimated to be 2600 $\mu J/cm^2$. Although no damage in the form of burning was observed up to this fluence level, the sample occasionally needed slight repositioning to restore mode-locked operation. A SWCNT-SA with a higher modulation depth should further enable self-starting mode-locked operation of the laser.

The net round trip GDD of the resonator was also calculated as $-58\ fs^2$ by using the soliton-area theorem [47],

$$W\tau = \frac{4|D|}{\gamma} \qquad \text{3-1}$$

where W is the intracavity pulse energy, τ is the measured pulse width divided by 1.76, D is the round trip cavity GDD, and γ is the nonlinearity coefficient given as

$$\gamma = \frac{2\pi}{\lambda}\left[n_2^{LiSAF}\frac{2L_{LiSAF}}{A_{eff}^{LiSAF}} + n_2^{fused}\frac{2L_{fused}}{A_{eff}^{fused}}\right] \qquad \text{3-2}$$

for this experiment. Above n_2^{LiSAF}, n_2^{fused} are the nonlinear refractive indices of the Cr:LiSAF and the fused silica substrate, A_{eff}^{LiSAF}, A_{eff}^{fused} are the effective beam areas in the Cr:LiSAF and the fused silica substrate, and L_{LiSAF}, L_{fused} are the length of the Cr:LiSAF and the fused silica substrate. In this calculation, the effective γ was further estimated as $5.8 \times 10^{-7}\ W^{-1}$ by using the nonlinear refractive indices of the Cr:LiSAF gain medium ($0.8 \times 10^{-16}\ cm^2$ / W [48]) and fused silica substrate ($2.48 \times 10^{-16}\ cm^2$ / W [49]). The estimates of the total GDD based on the soliton area theorem (−58 fs^2) and dispersion of the optics (−62 fs^2) were in good agreement.

To test whether the SWCNT-SA puts any limitation to the obtainable pulse widths, pulse generation was initiated by KLM. In this experiment, the SWCNT-SA was replaced with a bare fused silica substrate of the same thickness, and all cavity parameters were kept constant except for the position of M2, which was optimized to initiate KLM operation [See Figure 3-2]. Note also that M2 location was always away from the KLM operating point when mode locking was initiated with the SWCNT-SA. Typically, the stability range for mode-locking with SWCNT-SA is much broader than the KLM case. In the KLM experiments, the pulse width was again measured to be 21 fs, showing that the SWCNT-SA is not a limiting factor in obtaining short pulses at least down to 21 fs. This implies, once initiated (either by KLM or SA action), the pulse width depends on dispersion, nonlinearity and pulse energy, as expected from the soliton area theorem.

In conclusion, the direct generation of the shortest pulses from a SWCNT-SA mode-locked solid-state laser was achieved. At the pump power of 210 mW, the diode-pumped Cr:LiSAF laser produced 21 fs pulses with pulse energies of 0.18 nJ. In addition to the mode locking experiments, the steady-state and time-resolved optical characterizations were also performed to determine the passive loss, relaxation times, modulation depth, and saturation fluence of the SWCNT-SA. Comparing with KLM operation, mode locking with SWCNT-SA did not pose any limitation in obtainable pulse widths at least down to 21 fs. Further optimization of cavity GDD as well as power scaling with higher power pump diodes should lead to even shorter pulses that have been obtained by using other techniques.

Chapter 4
CONCLUSIONS

The central theme of this thesis study [See Chapter 3] was to test the short pulse generating capability of SWCNT-SAs. For achieving this objective, a Cr:LiSAF laser was chosen since they have a sufficiently broad gain bandwidth to produce 10-fs pulses [15]. The SWCNT-SA used in the experiments had a nonlinear absorption in the wavelength range coinciding with the gain bandwidth of Cr:LiSAF. At the pump power of 210 mW and mode-locked output power of 8.6 mW, the shortest pulses of 21 fs were obtained. This pulse width also represents the shortest pulses among the directly generated pulses from SWCNT-SA mode-locked solid state and fiber lasers. Further KLM experiments were conducted to verify that the limiting factor for obtaining shorter pulses was not the SWCNT-SA but possibly the cavity mirrors which was not optimized for higher wavelengths.

Another experimental work undertaken was the characterization of continuous-wave Cr:LiSAF laser at 850 nm, which was discussed in Chapter 2. For this purpose, the transmission values of different output couplers were measured carefully. Then, in Section 2.3, the threshold powers and power efficiencies of Cr:LiSAF laser with these output couplers were measured and presented in detail. Section 2.4 proceeded with the brief analysis of the experimental data and found an emission cross section - fluorescence lifetime product for Cr:LiSAF gain medium, which is in fair agreement with the reported data in the literature. The strange behaviour of the $P_{th}\eta/T$ vs T plot as it was already mentioned requires additional investigations to determine if it was just an experimental error or power-degrading mechanisms play a role in Cr:LiSAF lasers.

To have an understanding of the experimental material discussed in Chapter 2 and 3, the background materials were provided in Chapter 1. Section 1.1 and 1.2 were devoted to the essential components of the experiments, a Cr:LiSAF gain medium and SWCNT saturable absorber. The former was used obtain lasing at 850 nm and the latter was used to achieve pulsed operation. Sections 1.3-1.6 introduced the theoretical material in a concise form to be able to follow continuous-wave and mode locking experiments. The last section outlined the interferometric autocorrelator used to measure the duration of the pulses obtained in mode-locking experiments.

VITA

Gökhan Tanısalı was born in Istanbul in 1993. He received his BS degree in Physics and Mathematics from Koç University in 2017. He was then admitted to the MS program in Physics in the same university in 2017 and worked in the Laser Research Laboratory during his MS studies.

Publications:

- G. Tanisali, I. Baylam, M. Tasci, J. E. Bae, F. Rotermund, U. Demirbas, and A. Sennaroglu, "21 fs Cr:LiSAF laser mode locked with a single-walled carbon nanotube saturable absorber," Opt. Lett. 44, 4662-4665 (2019).

Proceedings:

- G. Tanisali, I. Baylam, F. Canbaz, J. E. Bae, F. Rotermund, U. Demirbas, and A. Sennaroglu, "Generation of 23-fs Pulses at 850 nm from a Carbon Nanotube Mode-Locked Solid-State Laser", Advanced Solid-State Lasers Conference, Vienna, Austria, September 29 – October 3, 2019, Oral Presentation.

- G. Tanisali, I. Baylam, M. Tasci, J. Bae, F. Rotermund, U. Demirbas, and A. Sennaroglu, “Direct Generation of the Shortest Pulses from a SWCNT-SA Mode-Locked Solid State Laser”, 21st Workshop on Optics, Electro-Optics and Photonics, Poster Presentation, Istanbul, Turkey, September 6, 2019.

BIBLIOGRAPHY

1. G. Robertson, D. Armstrong, M. J. P. Dymott, A. I. Ferguson, and G. L. Hogg, "Two-photon fluorescence microscopy with a diode-pumped Cr:LiSAF laser," Appl. Optics. **36**, 2481-2483 (1997).
2. S. A. Payne, L. L. Chase, L. K. Smith, W. L. Kway, and H. W. Newkirk, "Laser Performance of $LiSrAlF_6:Cr^{3+}$," J. Appl. Phys. **66**, 1051-1056 (1989).
3. R. Scheps, J. F. Myers, H. B. Serreze, A. Rosenberg, R. C. Morris, and M. Long, "Diode-Pumped $Cr:LiSrAlF_6$ Laser," Opt. Lett. **16**, 820-822 (1991).
4. A. Miller, P. Likamwa, B. H. T. Chai, and E. W. Vanstryland, "Generation of 150-Fs Tunable Pulses in $Cr:LiSrAlF_6$," Opt. Lett. **17**, 195-197 (1992).
5. J. M. Evans, D. E. Spence, W. Sibbett, B. H. T. Chai, and A. Miller, "50-Fs Pulse Generation from a Self-Mode-Locked $Cr:LiSrAlF_6$ Laser," Opt. Lett. **17**, 1447-1449 (1992).
6. G. J. Valentine, J. M. Hopkins, P. LozaAlvarez, G. T. Kennedy, W. Sibbett, D. Burns, and A. Valster, "Ultralow-pump-threshold, femtosecond $Cr^{3+}:LiSrAlF_6$ laser pumped by a single narrow-stripe AlGaInP laser diode," Opt. Lett. **22**, 1639-1641 (1997).
7. S. Tsuda, W. H. Knox, and S. T. Cundiff, "High efficiency diode pumping of a saturable Bragg reflector-mode-locked Cr:LiSAF femtosecond laser," Appl. Phys. Lett. **69**, 1538-1540 (1996).
8. J. M. Hopkins, G. J. Valentine, W. Sibbett, J. A. der Au, F. Morier-Genoud, U. Keller, and A. Valster, "Efficient, low-noise, SESAM-based femtosecond $Cr^{3+}:LiSrAlF_6$ laser," Opt. Commun. **154**, 54-58 (1998).
9. B. Agate, B. Stormont, A. J. Kemp, C. T. A. Brown, U. Keller, and W. Sibbett, "Simplified cavity designs for efficient and compact femtosecond Cr:LiSAF lasers," Opt. Commun. **205**, 207-213 (2002).
10. J. M. Hopkins, G. J. Valentine, B. Agate, A. J. Kemp, U. Keller, and W. Sibbett, "Highly compact and efficient femtosecond Cr:LiSAF lasers," IEEE J. Quant. Elect. **38**, 360-368 (2002).
11. R. P. Prasankumar, Y. Hirakawa, A. M. Kowalevicz, F. X. Kaertner, J. G. Fujimoto, and W. H. Knox, "An extended cavity femtosecond Cr : LiSAF laser pumped by low cost diode lasers," Opt Express **11**, 1265-1269 (2003).
12. U. Demirbas, D. Li, J. R. Birge, A. Sennaroglu, G. S. Petrich, L. A. Kolodziejski, F. X. Kartner, and J. G. Fujimoto, "Low-cost, single-mode diode-pumped Cr:Colquiriite lasers," Opt. Express **17**, 14374-14388 (2009).
13. D. Li, U. Demirbas, J. R. Birge, G. S. Petrich, L. A. Kolodziejski, A. Sennaroglu, F. X. Kartner, and J. G. Fujimoto, "Diode-pumped passively mode-locked GHz femtosecond Cr:LiSAF laser with kW peak power," Opt. Lett. **35**, 1446-1448 (2010).
14. S. Uemura and K. Torizuka, "Generation of 12-fs pulses from a diode-pumped Kerr-lens mode-locked Cr:LiSAF laser," Opt. Lett. **24**, 780-782 (1999).
15. S. Uemura and K. Torizuka, "Generation of 10 fs pulses from a diode-pumped Kerr-lens mode-locked Cr:LiSAF laser," Jpn. J. Appl. Phys. 1 **39**, 3472-3473 (2000).
16. A. Agnesi, F. Pirzio, E. Ugolotti, S. Y. Choi, D. I. Yeom, and F. Rotermund, "Femtosecond single-mode diode-pumped Cr:LiSAF laser mode-locked with single-walled carbon nanotubes," Opt. Commun. **285**, 742-745 (2012).
17. F. Canbaz, N. Kakenov, C. Kocabas, U. Demirbas, and A. Sennaroglu, "Graphene mode-locked Cr:LiSAF laser at 850 nm," Opt. Lett. **40**, 4110-4113 (2015).
18. F. Canbaz, N. Kakenov, C. Kocabas, U. Demirbas, and A. Sennaroglu, "Generation of sub-20-fs pulses from a graphene mode-locked laser," Opt. Express **25**, 2834-2839 (2017).

19. S. A. Payne, L. K. Smith, R. J. Beach, B. H. T. Chai, J. H. Tassano, L. D. Deloach, W. L. Kway, R. W. Solarz, and W. F. Krupke, "Properties of $Cr:LiSrAlF_6$ Crystals for Laser Operation," Appl. Optics **33**, 5526-5536 (1994).
20. J. K. Jabczynski, W. Zendzian, Z. Mierczyk, and Z. Frukacz, "Chromium-doped LiCAF laser passively Q switched with a V^{3+}: YAG crystal," Appl. Optics **40**, 6638-6645 (2001).
21. S. A. P. Lloyd L. Chase, "New tunable solid-state lasers $Cr3+:LiCaAIF_6$ and $Cr3+:LiSrAIF_6$," Optics & Photonics News, 16,17,18,19 (1990).
22. U. Demirbas and I. Baali, "Power and efficiency scaling of diode pumped Cr:LiSAF lasers: 770-1110 nm tuning range and frequency doubling to 387-463 nm," Opt. Lett. **40**, 4615-4618 (2015).
23. G. Tanisali, I. Baylam, M. Tasci, J. E. Bae, F. Rotermund, U. Demirbas, and A. Sennaroglu, "21 fs Cr:LiSAF laser mode locked with a single-walled carbon nanotube saturable absorber," Opt. Lett. **44**, 4662-4665 (2019).
24. F. Druon, F. Balembois, and P. Georges, "New laser crystals for the generation of ultrashort pulses," Cr. Phys. **8**, 153-164 (2007).
25. E. Sorokin, "Solid-state materials for few-cycle pulse generation and amplification," Top. Appl. Phys. **95**, 3-71 (2004).
26. W. Koechner, *Solid-State Laser Engineering,* Sixth Revised and Updated ed., Optical Sciences (Springer, 2006).
27. S. Iijima, "Helical Microtubules of Graphitic Carbon," Nature **354**, 56-58 (1991).
28. P. Avouris, M. Freitag, and V. Perebeinos, "Carbon-nanotube photonics and optoelectronics," Nat. Photonics **2**, 341-350 (2008).
29. N. A. T. Sebastien Nanot, Ji-Hee Kim, Xuan Wang, William D. Rice, Erik H. Hároz, Yogeeswaran Ganesan, Cary L. Pint, Junichiro Kono, *Handbook of Nanomaterials* (Springer, 2013).
30. T. W. Odom, J. L. Huang, and C. M. Lieber, "Single-walled carbon nanotubes - From fundamental studies to new device concepts," Ann. Ny. Acad. Sci. **960**, 203-215 (2002).
31. R. Saito, M. Fujita, G. Dresselhaus, and M. S. Dresselhaus, "Electronic-Structure of Chiral Graphene Tubules," Appl. Phys. Lett. **60**, 2204-2206 (1992).
32. W. B. Cho, J. H. Yim, S. Y. Choi, S. Lee, A. Schmidt, G. Steinmeyer, U. Griebner, V. Petrov, D. I. Yeom, K. Kim, and F. Rotermund, "Boosting the Nonlinear Optical Response of Carbon Nanotube Saturable Absorbers for Broadband Mode-Locking of Bulk Lasers," Adv. Funct. Mater. **20**, 1937-1943 (2010).
33. I. H. Baek, S. Y. Choi, H. W. Lee, W. B. Cho, V. Petrov, A. Agnesi, V. Pasiskevicius, D. I. Yeom, K. Kim, and F. Rotermund, "Single-walled carbon nanotube saturable absorber assisted high-power mode-locking of a Ti:sapphire laser," Opt. Express **19**, 7833-7838 (2011).
34. I. Baylam, S. Ozharar, H. Cankaya, S. Y. Choi, K. Kim, F. Rotermund, U. Griebner, V. Petrov, and A. Sennaroglu, "Energy scaling of a carbon nanotube saturable absorber mode-locked femtosecond bulk laser," Opt. Lett. **37**, 3555-3557 (2012).
35. D. Okazaki, H. Arai, A. Anisimov, E. I. Kauppinen, S. Chiashi, S. Maruyama, N. Saito, and S. Ashihara, "Self-starting mode-locked Cr:ZnS laser using single-walled carbon nanotubes with resonant absorption at 2.4 mu m," Opt. Lett. **44**, 1750-1753 (2019).
36. A. Schmidt, P. Koopmann, G. Huber, P. Fuhrberg, S. Y. Choi, D. I. Yeom, F. Rotermund, V. Petrov, and U. Griebner, "175 fs Tm:Lu2O3 laser at 2.07 mu m mode-locked using single-walled carbon nanotubes," Opt. Express **20**, 5313-5318 (2012).
37. F. Rotermund, W. B. Cho, S. Y. Choi, I. H. Baek, J. H. Yim, S. Lee, A. Schmidt, G. Steinmeyer, U. Griebner, D. I. Yeom, K. Kim, and V. Petrov, "Mode-locking of solid-state lasers by single-walled carbon-nanotube based saturable absorbers," Quantum Electron. **42**, 663-670 (2012).

38. W. B. Cho, J. H. Yim, S. Y. Choi, S. Lee, U. Griebner, V. Petrov, and F. Rotermund, "Mode-locked self-starting Cr:forsterite laser using a single-walled carbon nanotube saturable absorber," Opt. Lett. **33**, 2449-2451 (2008).

39. S. D. D. Cafiso, E. Ugolotti, A. Schmidt, V. Petrov, U. Griebner, A. Agnesi, W. B. Cho, Y. G. Zhang, S. Y. Choi, F. Rotermund, G. Reali, and F. Pirzio, "Sub-50 fs mode-locking of a Cr:YAG laser using an SWCNT-SA," Laser Phys. Lett. **10**(2013).

40. C. We, Y. J. Lyu, H. X. Shi, Z. Kang, H. Zhang, G. S. Qin, and Y. Liu, "Mid-Infrared Q-Switched and Mode-Locked Fiber Lasers at 2.87 μm Based on Carbon Nanotube," IEEE J. Sel. Top. Quant. **25** (2019).

41. A. Sennaroğlu, *Photonics and Laser Engineering: Principles, Devices, and Applications* (The McGraw-Hill, 2010).

42. D. H. Sutter, G. Steinmeyer, L. Gallmann, N. Matuschek, F. Morier-Genoud, U. Keller, V. Scheuer, G. Angelow, and T. Tschudi, "Semiconductor saturable-absorber mirror-assisted Kerr-lens mode-locked Ti : sapphire laser producing pulses in the two-cycle regime," Opt. Lett. **24**, 631-633 (1999).

43. F. A.-B. E. Nava-Palomares, S. Camacho-López, M. Fernández-Guasti, "Pulsed World," in *Laser Pulses: Theory, Technology, and Applications*, I. Peshko, ed. (InTech, 2012).

44. L. K. Smith, S. A. Payne, W. L. Kway, L. L. Chase, and B. H. T. Chai, "Investigation of the Laser Properties of Cr^{3+}: $LiSrGaF_6$," IEEE J. Quant. Elect. **28**, 2612-2618 (1992).

45. A. Sennaroglu, "Classification of power-degrading mechanisms in an optically pumped four-level laser: an analytical approach," J. Opt. Soc. Am. B **36**, 2202-2209 (2019).

46. I. Baylam, M. N. Cizmeciyan, N. Kakenov, C. Kocabas, and A. Sennaroglu, "Ultrafast spectroscopy of voltage reconfigurable graphene saturable absorbers in the visible and near infrared," 2D Mater. **6** (2019).

47. H. A. Haus, "Mode-locking of lasers," IEEE J. Sel. Top. Quant. **6**, 1173-1185 (2000).

48. I. T. Sorokina and K. L. Vodopyanov, *Solid-State Mid-Infrared Laser Sources* Topics in Applied Optics (Springer, 2003), Vol. 89.

49. D. Milam, "Review and assessment of measured values of the nonlinear refractive-index coefficient of fused silica," Appl. Optics **37**, 546-550 (1998).